



The Evolution of the Lyman-alpha Luminosity Function during Reionization

Alexa M. Morales^{1,2} , Charlotte A. Mason^{2,7} , Sean Bruton³, Max Gronke^{4,7} , Francesco Haardt^{5,6} , and Claudia Scarlata³ ¹Florida International University, 11200 SW 8th Street, Miami, FL 33199, USA; amora250@fiu.edu²Center for Astrophysics | Harvard & Smithsonian, 60 Garden Street, Cambridge, MA 02138, USA³Minnesota Institute for Astrophysics, University of Minnesota, 116 Church Street SE, Minneapolis, MN 55455, USA⁴Department of Physics & Astronomy, Johns Hopkins University, Baltimore, MD 21218, USA⁵DiSAT, Università dell'Insubria, via Valleggio 11, 22100 Como, Italy⁶National Institute of Nuclear Physics INFN, Milano—Bicocca, Piazza della Scienza 3, 20126 Milano, Italy

Received 2021 January 4; revised 2021 June 10; accepted 2021 July 1; published 2021 October 1

Abstract

The time frame in which hydrogen reionization occurred is highly uncertain, but can be constrained by observations of Lyman-alpha ($\text{Ly}\alpha$) emission from distant sources. Neutral hydrogen in the intergalactic medium (IGM) attenuates $\text{Ly}\alpha$ photons emitted by galaxies. As reionization progressed the IGM opacity decreased, increasing $\text{Ly}\alpha$ visibility. The galaxy $\text{Ly}\alpha$ luminosity function (LF) is thus a useful tool to constrain the timeline of reionization. In this work, we model the $\text{Ly}\alpha$ LF as a function of redshift, $z = 5\text{--}10$, and average IGM neutral hydrogen fraction, $\bar{x}_{\text{H I}}$. We combine the $\text{Ly}\alpha$ luminosity probability distribution obtained from inhomogeneous reionization simulations with a model for the UV LF to model the $\text{Ly}\alpha$ LF. As the neutral fraction increases, the average number density of $\text{Ly}\alpha$ emitting galaxies decreases, and are less luminous, though for $\bar{x}_{\text{H I}} \lesssim 0.4$ there is only a small decrease in the $\text{Ly}\alpha$ LF. We use our model to infer the IGM neutral fraction at $z = 6.6, 7.0$, and 7.3 from observed $\text{Ly}\alpha$ LFs. We conclude that there is a significant increase in the neutral fraction with increasing redshift: $\bar{x}_{\text{H I}}(z = 6.6) = 0.08^{+0.08}_{-0.05}$, $\bar{x}_{\text{H I}}(z = 7.0) = 0.28 \pm 0.05$ and $\bar{x}_{\text{H I}}(z = 7.3) = 0.83^{+0.06}_{-0.07}$. We predict trends in the $\text{Ly}\alpha$ luminosity density and Schechter parameters as a function of redshift and the neutral fraction. We find that the $\text{Ly}\alpha$ luminosity density decreases as the universe becomes more neutral. Furthermore, as the neutral fraction increases, the faint-end slope of the $\text{Ly}\alpha$ LF steepens, and the characteristic $\text{Ly}\alpha$ luminosity shifts to lower values; hence, we conclude that the evolving shape of the $\text{Ly}\alpha$ LF—not just its integral—is an important tool to study reionization.

Unified Astronomy Thesaurus concepts: Reionization (1383); Early universe (435); Intergalactic medium (813); Galaxy evolution (594); Lyman-alpha galaxies (978); Lyman-break galaxies (979); Luminosity function (942)

1. Introduction

After recombination, $\sim 75\%$ of the baryons in the early universe were atomic hydrogen. In the present-day universe, the majority of hydrogen in the intergalactic medium (IGM) is ionized. At some point within the first billion years, ionizing photons, likely emitted by the first stars and galaxies, reionized hydrogen during this *Epoch of Reionization*, initially in bubbles around galaxies, which eventually overlapped and created an entirely ionized IGM (e.g., Barkana & Loeb 2007; Mesinger 2016; Dayal & Ferrara 2018).

The time frame in which reionization occurred is still highly uncertain. Its onset and progression are rather poorly constrained (e.g., Greig et al. 2017; Mason et al. 2019). The best constraints currently come from observations of the increasing optical depth to Lyman-alpha ($\text{Ly}\alpha$) photons, observed in the spectra of high-redshift quasars (e.g., Fan et al. 2006; McGreer et al. 2015; Bañados et al. 2018; Davies et al. 2018; Greig et al. 2017) and galaxies—both those selected as Lyman-break galaxies (LBGs; e.g., Treu et al. 2013; Schenker et al. 2014; Mesinger et al. 2014; Mason et al. 2018, 2019; Hoag et al. 2019; Whitler et al. 2020; Jung et al. 2020) and $\text{Ly}\alpha$ emitters (e.g., Malhotra & Rhoads 2004; Konno et al. 2018). These constraints imply a fairly late and rapid reionization (e.g., Mason et al. 2019; Naidu et al. 2020), though c.f. Finkelstein et al. (2019) and Jung et al. (2020) who find evidence for a slightly earlier reionization. During reionization, $\text{Ly}\alpha$ photons are attenuated extremely

effectively by neutral hydrogen (e.g., Miralda-Escudé 1998; Mesinger et al. 2014; Mason et al. 2018). As a result, $\text{Ly}\alpha$ observations can be an investigative tool of the neutral IGM during the Epoch of Reionization. However, these reionization inferences are limited by systematic uncertainties in modeling the intrinsic $\text{Ly}\alpha$ emission—more independent probes are necessary to understand the systematic uncertainties in reionization inferences.

In this paper, we use the $\text{Ly}\alpha$ luminosity function (LF) to constrain the progression of reionization with cosmic time. $\text{Ly}\alpha$ LFs have been used for over a decade to understand reionization (e.g., Rhoads & Malhotra 2001; Malhotra & Rhoads 2004; Stern et al. 2005; Jensen et al. 2013). LFs describe the luminosity distribution of a population of objects and we can quantify their evolution by looking at the LF at different redshifts. As $\text{Ly}\alpha$ is typically expected to be the strongest emission line in the rest-frame optical to UV (e.g., Partridge & Peebles 1967; Shapley et al. 2003), wide-area ground-based narrow-band surveys (e.g., Malhotra & Rhoads 2004; Ota et al. 2008, 2010; Ouchi et al. 2010; Konno et al. 2014, 2016; Ota et al. 2017; Konno et al. 2018), and more recently, space-based grism observations (e.g., Tilvi et al. 2016; Bagley et al. 2017; Larson et al. 2018) have been efficient at discovering large populations of galaxies at high redshifts, selected based on strong $\text{Ly}\alpha$ fluxes, also referred to as *Ly α emitters* or LAEs.

As $\text{Ly}\alpha$ photons are obscured during reionization, a decline in the $\text{Ly}\alpha$ LF is a signature of an increasingly neutral IGM. However, any evolution must be disentangled from the

⁷ Hubble Fellow.

evolution in the underlying galaxy population with redshift (i.e., as galaxies become less numerous at high redshifts due to hierarchical structure formation). Previous works typically compared the evolution of the Ly α LF to that of the UV LF, which describes the number density of LBGs and is not distorted by reionization, to establish the evolution due to neutral gas (e.g., Ouchi et al. 2008, 2010; Konno et al. 2018, 2016). These works estimated the neutral fraction at specific redshifts by using the drop in the Ly α luminosity density (LD) compared to the UV LD to calculate a transmission fraction, T_{IGM} , the fraction of Ly α flux transmitted through the IGM, under the assumption T_{IGM} does not depend on Ly α or UV luminosity.

However, due to the inhomogeneous nature of reionization (e.g., Miralda-Escudé et al. 2000; Ciardi et al. 2003; Furlanetto & Oh 2005; Mesinger 2016), the transmission fraction is in reality a broad distribution, which is not captured by the LD estimates. Importantly, Mason et al. (2018) demonstrated that the transmission fraction depends on not only the average neutral fraction of hydrogen in the IGM, but also the galaxy’s local environment and emission properties. For example, UV-bright galaxies have higher transmission fractions at all neutral fraction values because their Ly α line profiles are typically redshifted far into the damping wing absorption profile and they also typically exist in large reionized bubbles early in reionization (Mason et al. 2018; Whittler et al. 2020). By contrast, UV-faint galaxies emit Ly α closer to their systemic velocity, which is thus more significantly absorbed by surrounding neutral IGM. They can be found in under-dense regions of the cosmic web where the IGM is still neutral, resulting in a lower transmission fraction even for high average neutral fractions.

This work models the evolution of the Ly α LF as a function of the volume average neutral hydrogen fraction, x_{H} , and redshift, z , to interpret observations and constrain reionization. We create our model by convolving the UV LF with the Ly α luminosity probability distribution as a function of M_{UV} . The models in this project include realistic, inhomogeneous simulations for reionization, enabling us to include the full distribution of Ly α transmissions. This is an improvement on previous work that interpreted the Ly α LF using fixed Ly α transmission fractions (e.g., Konno et al. 2018; Hu et al. 2019), which may be considered an oversimplification. Furthermore, we use an analytic approach that enables us to model the Ly α LF as a function of x_{H} and z independently, rather than using a simulation with a fixed reionization history (e.g., Itoh et al. 2018)—allowing us to disentangle the impact of IGM and redshift evolution.

This paper is structured as follows. In Section 2, we describe our model for the Ly α LF. In Section 3, we describe our results for the Ly α LF and the evolution of the Schechter function parameters and LD. We infer the evolution of the neutral fraction for $z > 6$ by fitting our model to observations and we forecast predictions for future surveys with the Nancy Grace Roman Space Telescope (NGRST), Euclid, and the James Webb Space Telescope (JWST). In Section 4, we discuss our results and we present our conclusions in Section 5.

We use the Planck Collaboration et al. (2016) cosmology and all magnitudes are given in the AB system.

2. Methods

Here, we describe the components of our model. In Section 2.1, we describe the methodology used to model the

Ly α LF. Both model components—the Ly α luminosity probability distribution and the UV LF—are described in the succeeding Sections 2.1.1 and 2.2. Section 2.3 describes the normalization of the Ly α LF. Section 2.4 describes the Bayesian framework used to infer the neutral fraction given the Ly α LF model and observational data. In Section 2.5, we discuss the differences in observational data sets that led to omitting or including certain surveys in our analysis.

2.1. Modeling the Ly α LF

We model the evolution of the Ly α LF as a function of redshift and x_{H} by convolving models for the Ly α emission from LBGs and the UV LF during reionization. This enables us to disentangle the effects of redshift evolution from the evolution due to IGM absorption (Mason et al. 2015b; Mesinger 2016; Mason et al. 2018).

The LF of galaxies shows the number density of galaxies in a certain luminosity interval and is typically described using the Schechter (1976) function:

$$\phi(L)dL = \phi^* \left(\frac{L}{L^*} \right)^\alpha \exp\left(-\frac{L}{L^*}\right) d\left(\frac{L}{L^*}\right), \quad (1)$$

where ϕ^* is the normalization constant, α is the power law for faint-end slope for $L < L^*$, and there is an exponential cutoff at $L > L^*$. These parameters are known to be conditional on the observed wavelength and cosmic time, as well as the type of galaxy (e.g., Dahlen et al. 2005). The rest-frame UV LF has been measured in detail out to $z \sim 10$ and is one of our best tools for studying the evolution of galaxy populations (e.g., Bouwens et al. 2016, 2015; Finkelstein et al. 2015; Oesch et al. 2015).

Following Dijkstra & Wyithe (2012) and Gronke et al. (2015) we can predict the number density of LAEs by using the UV LF and Ly α luminosity probability distribution for LBGs to model the Ly α LF:

$$\phi_{\text{LAE}}(L_\alpha, x_{\text{H}}, z) dL_\alpha = dL_\alpha F \times \int_{M_{\text{UV},\text{min}}}^{M_{\text{UV},\text{max}}} dM_{\text{UV}} \phi(M_{\text{UV}}, z) P(L_\alpha | M_{\text{UV}}, x_{\text{H}}, z). \quad (2)$$

Here, $\phi(M_{\text{UV}}, z) dM_{\text{UV}}$ is the UV LF in the range $M_{\text{UV}} \pm dM_{\text{UV}}/2$ and is described in Section 2.2. $P(L_\alpha | M_{\text{UV}}, x_{\text{H}})$, is the conditional probability of galaxies that have a Ly α luminosity L_α in $L_\alpha \pm dL_\alpha/2$, given a M_{UV} value and neutral fraction and is described in Section 2.1.1. We integrate our Ly α LF over the M_{UV} range $-24 < M_{\text{UV}} < -12$ covering the observed range of the UV LF, $-23 < M_{\text{UV}} < -17$.

The factor F in Equation (16) is a normalization constant to fit the LF model to observations and can be thought of as the ratio of predicted LAEs versus the total number of LAEs recorded. If the Ly α luminosity distribution, $P(L_\alpha | M_{\text{UV}}, x_{\text{H}}, z)$, accurately describes the luminosities of the same LBGs measured in the UV LF this factor should be $F=1$ (See Section 4.3 for further discussion).

2.1.1. Ly α Luminosity Probability Distribution

The probability distribution for Ly α luminosity is derived from the Ly α rest-frame equivalent width (EW) probability density function $P(\text{EW} | M_{\text{UV}})$, where $P(L_\alpha | M_{\text{UV}}, x_{\text{H}}) = P(\text{EW} | M_{\text{UV}}, x_{\text{H}}) \frac{\partial \text{EW}}{\partial L_\alpha}$. We use the rest-frame EW probability distribution models by Mason et al. (2018) (based on

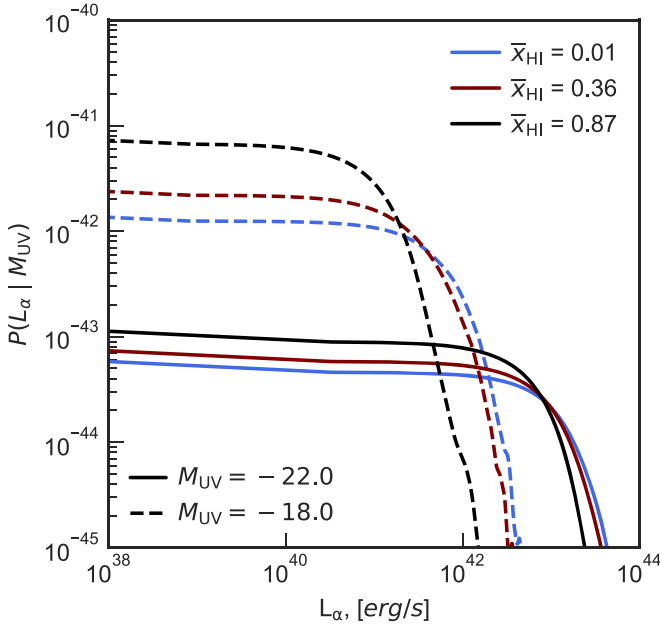


Figure 1. Example of the probability distribution for $\text{Ly}\alpha$ luminosity, $P(\text{Ly}\alpha | M_{\text{UV}}, x_{\text{HI}})$. This distribution is for UV-bright (solid line) and UV-faint galaxies (dashed line) at different x_{HI} values, $x_{\text{HI}} = 0.01, 0.36$, and 0.87 . When x_{HI} increases to an almost neutral environment, the probability of detecting luminous $\text{Ly}\alpha$ galaxies decreases compared to in an almost fully ionized environment.

observations by De Barros et al. (2017) who forward-model observed EW after transmission through 1.6 Gpc^3 inhomogeneous reionization simulations (Mesinger 2016) at fixed average neutral fraction $x_{\text{HI}} = 0.01 - 0.95$, with a spacing of $\Delta x_{\text{HI}} \sim 0.01 - 0.03$. We use the following relationship between $\text{Ly}\alpha$ luminosity in erg s^{-1} and EW to obtain $\partial \text{EW} / \partial L_\alpha$:

$$L_\alpha = \text{EW} \times L_{\text{UV},\nu} \times \frac{c}{\lambda_{\text{Ly}\alpha}^2} \left(\frac{\lambda_{\text{Ly}\alpha}}{\lambda_{\text{UV}}} \right)^{\beta+2} \quad (3)$$

Here, $\lambda_\alpha \sim 1216 \text{ \AA}$ is the wavelength of the $\text{Ly}\alpha$ resonance, the rest-frame wavelength of the UV continuum is typically measured at $\lambda_{\text{UV}} \sim 1500 \text{ \AA}$, β is the UV continuum slope, where we assume $\beta = -2$ typical for high redshifts (e.g., Bouwens et al. 2014), and c is the speed of light. $L_{\text{UV},\nu}$ is the UV LD:

$$L_{\text{UV},\nu} = 4\pi(10)^2 \times 10^{-0.4(M_{\text{UV}}+48.6)} \text{ erg s}^{-1} \text{ Hz}^{-1}. \quad (4)$$

We normalize $P(L_\alpha | M_{\text{UV}}, x_{\text{HI}})$ over the luminosity range $L_\alpha = 0 - 10^{44.5} \text{ erg s}^{-1}$ to encompass a large $\text{Ly}\alpha$ luminosity interval, and within our defined M_{UV} range between $-24 < M_{\text{UV}} < -12$ (see Section 2.1).

The $\text{Ly}\alpha$ luminosity probability distribution, $P(L_\alpha | M_{\text{UV}}, x_{\text{HI}})$, is shown in Figure 1 for a few x_{HI} and M_{UV} values. We note that as the Mason et al. (2018) models assume no evolution of the intrinsic $\text{Ly}\alpha$ EW distribution with redshift—the only redshift evolution is due to the increasing neutral fraction, our $\text{Ly}\alpha$ luminosity distribution models also depend only on x_{HI} with no additional redshift evolution. Recent works by Hashimoto et al. (2017), Jung et al. (2018), and Shibuya et al. (2018) confirm a suitable approach to the $\text{Ly}\alpha$ EW distribution models we incorporate into our work. Each paper ultimately notes no significant evolution in the $\text{Ly}\alpha$ EW distribution with respect to redshift for $z \sim 5-7$.

Figure 1 demonstrates large differences in the probability distribution for UV-bright and UV-faint galaxies. For UV-faint

galaxies, we expect a higher probability of $\text{Ly}\alpha$ luminosity emission at all x_{HI} values but with a $\text{Ly}\alpha$ luminosity cutoff at $L_\alpha \lesssim 10^{42} \text{ erg s}^{-1}$. For UV-bright galaxies, at all x_{HI} we expect galaxies to have higher $\text{Ly}\alpha$ luminosity values up to $L_\alpha \lesssim 10^{44} \text{ erg s}^{-1}$, but this is rarer. For both UV-bright and UV-faint galaxies, as the neutral fraction increases, the probability of galaxies emitting strong $\text{Ly}\alpha$ overall decreases.

The M_{UV} dependence of $P(L_\alpha | M_{\text{UV}})$ is a direct consequence of the EW distribution model by Mason et al. (2018). This model can be described as an exponential distribution plus a delta function:

$$P(\text{EW} | M_{\text{UV}}) = \frac{A(M_{\text{UV}})}{\text{EW}_c(M_{\text{UV}})} e^{-\frac{\text{EW}}{\text{EW}_c(M_{\text{UV}})}} H(\text{EW}) + [1 - A(M_{\text{UV}})] \delta(\text{EW}), \quad (5)$$

where

$$A(M_{\text{UV}}) = 0.65 + 0.1 \tanh[3(M_{\text{UV}} + 20.75)], \quad (6)$$

$$\text{EW}_c(M_{\text{UV}}) = 31 + 12 \tanh[4(M_{\text{UV}} + 20.25)] \text{ \AA} \quad (7)$$

account for the fraction of emitters and the anticorrelation of EW with M_{UV} , respectively. $H(\text{EW})$ is the Heaviside step function and $\delta(\text{EW})$ is a Dirac delta function (see Section 2.1.3 of Mason et al. 2018 for further details). The intrinsic, emitted, distribution (i.e., $x_{\text{HI}} = 0$) is an empirical model fit to observations by De Barros et al. (2017) at $z \sim 6$, where it was found that UV-bright galaxies had a lower probability of being emitters, and had lower average EWs (consistent with previous findings; e.g., Ando et al. 2006; Stark et al. 2010). The model EW distribution is then painted onto galaxies in inhomogeneous reionization simulations, with different average neutral fractions, and the *observed* EW distribution in each of those simulations is recovered by sampling the transmission along thousands of sightlines.

Although bright galaxies have low EW compared to faint galaxies, they are, on average, less affected by neutral gas in the IGM: UV-bright galaxies are typically more massive and reside in dense regions of the universe, in large IGM bubbles that have already reionized. In the simulations we use, reionization occurs first in over-dense regions due to the excursion set formalism (Mesinger & Furlanetto 2007; Mesinger 2016). Observationally, clustering analyses show that UV-bright galaxies typically live in massive halos in dense regions (e.g., Figure 15 of Harikane et al. 2018). So, $\text{Ly}\alpha$ photons can escape more easily and EWs decrease at a slower rate (transmissions are already high). UV-faint galaxies have a higher intrinsic EW, on average, that decreases more rapidly than for UV-bright galaxies as the universe becomes more neutral. This is because they can be more typically found in neutral patches of IGM.

As described above in Section 2.1, we generate our $\text{Ly}\alpha$ LF by integrating the UV LF over the M_{UV} range $-24 < M_{\text{UV}} < -12$, covering the observed range of the UV LF, $-23 \lesssim M_{\text{UV}} \lesssim -17$. As the Mason et al. (2018) EW models were defined for $-23 \leq M_{\text{UV}} \leq -17$ to include galaxies outside of this range we set galaxies brighter than $M_{\text{UV}} = -23$ to have the same $P(L_\alpha | M_{\text{UV}} = -23)$, and all galaxies fainter than $M_{\text{UV}} = -17$ have the same $P(L_\alpha | M_{\text{UV}} = -17)$ (for a given x_{HI}).

2.2. Galaxy UV LFs

In this paper, we use the Mason et al. (2015b) UV LF model. In this model galaxy evolution is dependent on star formation that is associated with the construction of dark matter halos,

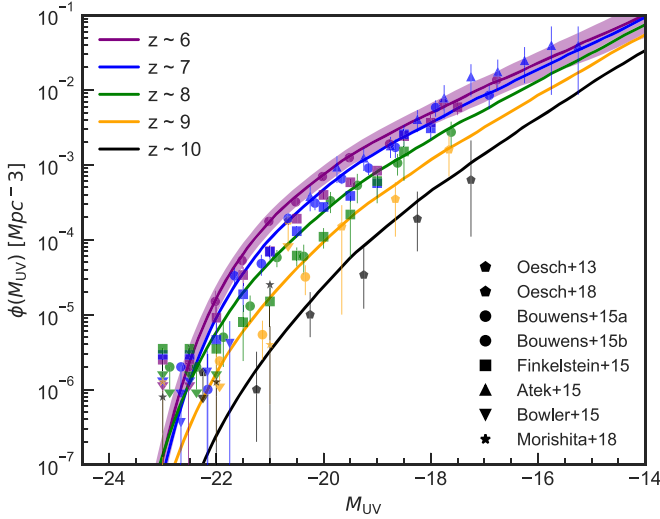


Figure 2. Modeled UV LF for redshifts at $z = 6$ – 10 for UV-bright and faint galaxies, based on Mason et al. (2015b) UV LF model. There is a steep, exponential, drop-off for UV-bright galaxies that turns over into a power-law slope for UV-faint galaxies. The shaded region shows the 1σ confidence range at $z \sim 6$ and similar regions can be assumed for each redshift. UV LF observations are shown with each marker color matching its corresponding UV LF model at a given redshift. Points show the binned UV LFs and upper limits from Oesch et al. (2013), Oesch et al. (2018), Bouwens et al. (2015), Bouwens et al. (2016), Finkelstein et al. (2015), Atek et al. (2015), Bowler et al. (2015), and Morishita et al. (2018).

with the assumption that these halos have a star formation efficiency that is mass dependent but redshift independent, which successfully reproduces observations over 13 Gyr (see also, e.g., Trenti et al. 2010; Tacchella et al. 2013, 2018; Mirocha et al. 2020).

The UV LF is plotted in Figure 2. It is well described by a Schechter (1976) function (Equation (1)). The steep drop-off of UV-bright galaxies can be explained in terms of rare high mass halos and their star formation efficiency: high mass halos are not efficient at forming stars, likely due to strong negative active galactic nuclei (AGN) feedback. The drop in number density with increasing redshift indicates a shift in star formation toward fainter, less massive galaxies.

2.3. Calibrating the Normalization of the Ly α LF

To obtain an accurate model of the Ly α LF to compare with observations, we must calibrate the Ly α LF by finding the normalization constant, F . This factor accounts for any over-prediction in the number density of LAEs caused by the Ly α luminosity distribution, $P(L_\alpha | M_{UV}, x_{H\text{I}}, z)$ (Dijkstra & Wyithe 2012; Gronke et al. 2015). If the Ly α luminosity distribution accurately describes the luminosities of the LBGs measured in the UV LF we should obtain $F = 1$.

We estimate F using a maximum-likelihood approach to fit our model at $z = 5.7$, $x_{H\text{I}} \sim 0$ to the Konno et al. (2018) and Ouchi et al. (2008) observations at $z = 5.7$. We set the calibration at this redshift and neutral fraction as it is likely to be after the end of reionization (e.g., McGreer et al. 2015). Note, due to our reionization simulation grid (see Section 2.1.1), we use $x_{H\text{I}} = 0.01$ for the calibration, rather than $x_{H\text{I}} = 0.0$, but note that the difference in $P(L_\alpha | M_{UV}, x_{H\text{I}})$ should be negligible for such a small change in neutral fraction (as shown by Mason et al. 2018).

We maximize the likelihood for the observed Ly α LFs in each luminosity bin L_i : $P(\phi_i | \theta = F, L_i, \sigma_i)$ given our model $\phi_{\text{mod}}(\theta = F, L)$. This estimation using binned LFs may not be the most optimal: a more accurate likelihood would be obtained using individual source information and the survey selection function (see, e.g., Trenti & Stiavelli 2008; Kelly et al. 2008; Schmidt et al. 2014; Mason et al. 2015a); however, collating these data is not feasible within the scope of this project, and we leave this for future works. We note that Trenti & Stiavelli (2008) demonstrated that LFs estimated from binned data are generally in good agreement with those measured from unbinned data, but can bias the faint-end slope toward steeper values. However, as the observed high-redshift Ly α LFs are mostly $\gtrsim L^*$, we do not expect this to have a large impact on our results as the faint end will already have large uncertainties.

Following Gillet et al. (2020) we use a split-norm likelihood (Equation (9)), to take into account asymmetric error bars. Assuming each observation and luminosity bin are independent, the total likelihood is

$$P(\phi_{\text{obs}} | \theta = F, L) = \prod_i S(\phi_{\text{mod}}(F, L_i), \mu_i, \sigma_{1,i}, \sigma_{2,i}). \quad (8)$$

Here, $\phi_{\text{mod}}(F, L_i)$ is the model LF at luminosity L_i for parameter $\theta = F$, μ_i is the observed number density value at L_i , and $\sigma_{1,i}$ and $\sigma_{2,i}$ are the respective lower and upper errors of the observed number density. In a single luminosity bin

$$S(\phi_{\text{mod}}) = \begin{cases} B \exp\left[-\frac{1}{2} \frac{(\phi_{\text{mod}} - \mu)^2}{\sigma_1^2}\right] & \text{if } \phi_{\text{mod}} \leq \mu \\ B \exp\left[-\frac{1}{2} \frac{(\phi_{\text{mod}} - \mu)^2}{\sigma_2^2}\right] & \text{if } \phi_{\text{mod}} \geq \mu \end{cases}, \quad (9)$$

$$B = \left[\sqrt{2\pi} \left(\frac{\sigma_1 + \sigma_2}{2} \right) \right]^{-1}. \quad (10)$$

We minimize the logarithm of the likelihood Equation (8) to find F using the Python package `SciPy minimize`. The obtained minimum value is $F = 0.974$, which we then use for Ly α LF at all redshifts and $x_{H\text{I}}$ values.

Our recovered value of $F \approx 1$ indicates our luminosity distribution is a good model for LBGs. Other works, such as Dijkstra & Wyithe (2012) and Gronke et al. (2015), found $F \sim 0.5$ at $z = 5.7$ and $F < 1$ at all lower redshifts, which is due to the different EW distribution they employed. We discuss this further in Section 4.3.

2.4. Bayesian Inference of the Neutral Fraction

In Section 3.5, we use our model to infer the IGM neutral fraction from observations.

Bayes' theorem allows us to establish a posterior distribution for $x_{H\text{I}}$ given observations. Bayes' theorem is defined as

$$P(x_{H\text{I}} | \{\phi_{\text{obs},i}(L_i)\}, z) = \frac{P(\{\phi_{\text{obs},i}(L_i)\} | x_{H\text{I}}, z) P(x_{H\text{I}} | z)}{P(\{\phi_{\text{obs},i}(L_i)\})}. \quad (11)$$

Here, $\{\phi_{\text{obs},i}(L_i)\}$ is the set of observed data in luminosity bins L_i (where μ_i is the observed number density value at L_i , and $\sigma_{1,i}$ and $\sigma_{2,i}$ are the respective lower and upper errors of the observed number density). $P(\{\phi_{\text{obs},i}(L_i)\} | x_{H\text{I}}, z)$ is the likelihood of obtaining our observed data given the model. $P(x_{H\text{I}} | z) = P(x_{H\text{I}})$ is the prior for the model parameter, $x_{H\text{I}}$,

where we assume the neutral fraction is independent of redshift. More physically, this prior could be dependent on redshift, but we leave the prior independent of redshift to allow more flexibility when estimating the neutral fraction. Regardless, we still see the inferred neutral fraction increase with redshift. We use a uniform prior from 0–1. Although this is technically not needed, making our approach essentially a maximum-likelihood estimate, we keep the Bayesian formalism to allow more physical priors to be used in future works. $P(\{\phi_{\text{obs},i}(L_i)\})$ is the Bayesian information that normalizes the posterior distribution.

We obtain the posterior distribution of the neutral fraction of hydrogen using our Ly α LF model given the observed Ly α luminosity values, L_α , number density, $\phi(L_\alpha)$, and the uncertainties in the number density. We use the same split-norm likelihood defined in Equation (8) with $\phi_{\text{mod}}(x_{\text{H}}, L_i)$. Further explanation of the inference of the neutral fraction can be seen in Appendix B.

We include uncertainties in our model Ly α LF due to uncertainties in the UV LF via a Monte Carlo approach. We generate 100 UV LFs with a 0.2 dex uncertainty in number density (estimated from the Mason et al. 2015b UV LF model). We then calculate the standard deviation of the resulting Ly α LF, σ_{mod} , as a function of Ly α luminosity. We find the standard deviation is well described by $\sigma_{\text{mod}}(L_\alpha) \approx 0.1 \times \phi_{\text{mod}}(L_\alpha)$. We use this uncertainty in calculating the likelihood (Equation (9)), where

$$\sigma_1 \rightarrow \sqrt{\sigma_1^2 + \sigma_{\text{mod}}^2}, \quad (12)$$

$$\sigma_2 \rightarrow \sqrt{\sigma_2^2 + \sigma_{\text{mod}}^2}. \quad (13)$$

2.5. Ly α LF Observational Data Sets

In comparing our model to observations, we wanted to ensure we used data sets where the selection strategies were similar to each other and similar to the data sets used to calibrate our model (Section 2.3), as it is known that different survey selection techniques can produce different estimates of the Ly α LF (for further discussion see Taylor et al. 2020). This led to the inclusion or exclusion of certain surveys from the estimation of the neutral fraction. In general, we aimed to use surveys that covered the widest areas (to minimize cosmic variance) and deepest Ly α luminosity limits.

For the neutral fraction inference (Section 3.5) it was important to use observed LFs that were calculated consistently with each other and our calibration LF at $z = 5.7$ (Section 2.3). As Konno et al. (2018) covers the largest area, we used their LF for our calibration. Therefore, for the neutral fraction inference, we included additional data sets that covered the largest redshift range with similar flux measurements and corrections for their systematic uncertainties.

The observational data sets we used to infer the neutral fraction, and their survey areas are as follows: Ly α LFs at $z = 5.7$ and 6.6 by Konno et al. (2018), who surveyed ~ 13.8 and $\sim 21.2 \text{ deg}^2$ areas of the sky using Subaru/Hyper Suprime-Cam (HSC) Subaru Strategic Program Survey for redshifts $z = 5.7$ and 6.6, respectively, and by Ouchi et al. (2008, 2010), who surveyed a 1 deg^2 area of the sky using Subaru/XMM-Newton Deep Survey (SXDS) fields for both redshifts $z = 5.7$ and 6.6. At $z = 7.0$, we used Ly α LFs observed by Ota et al. (2017), who measured the total effective area of the Subaru Deep Field (SDF) and SXDS survey images for LF candidates

to be $\sim 0.5 \text{ deg}^2$. Itoh et al. (2018) conducted an ultra-deep and large-area HSC imaging survey under the Cosmic HydrOgen Reionization Unveiled with Subaru Program in a total of 3.1 deg^2 using two independent blank fields. Finally, Hu et al. (2019) implemented a large-area survey using the Lyman Alpha Galaxies in the Epoch of Reionization project’s deep-fields Cosmic Evolution Survey (COSMOS) and Chandra Deep Field South (CDFs) covering an effective area of 2.14 deg^2 . Ly α LFs $z = 7.3$ are identified by Konno et al. (2014), who surveyed a $\sim 0.5 \text{ deg}^2$ area in the SXDS and COSMOS fields and Shibuya et al. (2012), who surveyed a total area of 1719 arcmin^2 ($\sim 0.5 \text{ deg}^2$) in the SDF and the Subaru/XMM-Newton Deep Survey Field (SXDF), using the Suprime-Cam.

We ultimately excluded LFs measured by Santos et al. (2016) at $z = 5.7$ and 6.6 when estimating the neutral fraction because these LFs were significantly higher than those by Konno et al. (2018) and Ouchi et al. (2008, 2010). This is most likely due to differences in incompleteness corrections and the methodology for taking Ly α flux measurements from narrow-band images (see Santos et al. 2016; Konno et al. 2018, for further discussion). We also excluded the LFs measured by Taylor et al. (2020) at $z = 6.6$ from the estimation of the neutral fraction, where unlike other works, they corrected for a selection incompleteness; however, our model only incorporates observations uncorrected for selection incompleteness (this decision is discussed further in Section 3.2).

Although there are Ly α LF measurements at higher redshift values (e.g., Hibon et al. 2010; Tilvi et al. 2010; Krug et al. 2012; Clément et al. 2012; Matthee et al. 2014, at $z = 7.7$), we decide not to include these works in comparison to our model. Ultimately, the areas of surveys greater than $z = 7.3$ are much smaller than surveys completed at lower redshifts. Therefore, surveys at $z > 7.3$ more likely to be biased because reionization is inhomogeneous (see, e.g., Figure 11 from Jensen et al. 2013, where they compare LFs for different survey areas). The highest redshift LAE candidates are also prone to higher rates of contamination (Matthee et al. 2014), so with only the inclusion of lower redshifts, we can obtain more robust estimations of the neutral fraction.

3. Results

In this section, we describe the evolution of our model for the Ly α LF. In Section 3.1, we describe the expectation value of Ly α luminosity at a given M_{UV} to understand what region of the Ly α LF galaxies from a given UV magnitude range dominate. In Section 3.2, we present our predicted Ly α LF and compare with observations. In Section 3.3, we describe the evolution of the Schechter parameters for our Ly α LF model from $z = 5$ –10. In Section 3.4, we show our results for the Ly α LD as a function of redshift and x_{H} . In Section 3.5, we present our inference of the IGM neutral fraction. Section 3.6 presents predictions for future surveys with NGRST, Euclid, and JWST from our model.

3.1. The Average Ly α Luminosity of LBGs

To understand the impact of environment and galaxy properties on the evolution of the Ly α LF during reionization, we investigate the typical Ly α luminosity of LBGs. In Figure 3, we plot the expectation value of Ly α luminosity, $\langle L_\alpha \rangle$, as a function of UV magnitude at $z = 6.0$. The

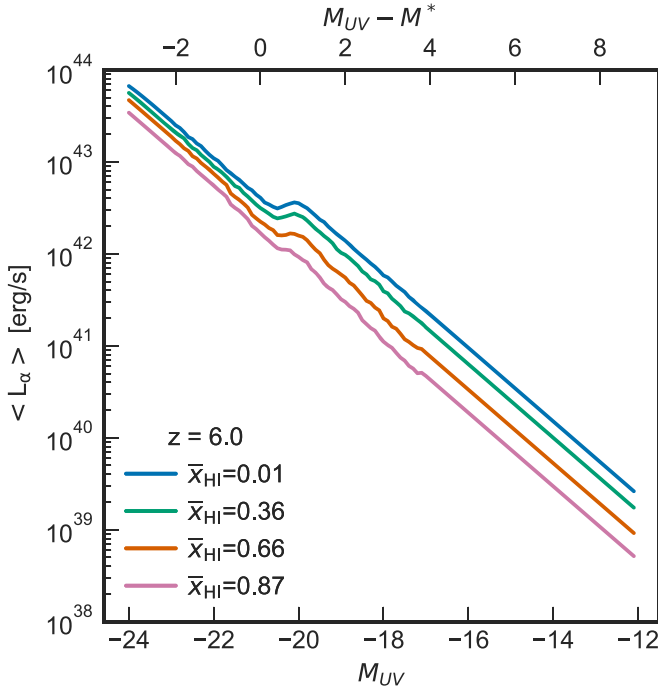


Figure 3. Expectation value for $\text{Ly}\alpha$ luminosity at $z = 6.0$ for a range of M_{UV} values and x_{HI} values. Here, we also show how $\langle L_\alpha \rangle$ compares for galaxies brighter or fainter than M_{UV}^* (where we use $M_{\text{UV}}^* = -20.9$ at $z = 6.0$ from Mason et al. 2015b). The model expects UV-faint galaxies to have an average $\text{Ly}\alpha$ luminosity lower than that of UV-bright galaxies. As the neutral fraction increases, $\langle L_\alpha \rangle$ decreases. For UV-bright galaxies, there is not much decrease in the $\text{Ly}\alpha$ luminosity expected (a factor of ~ 2), compared to a factor of ~ 10 for UV-faint galaxies. The bump in the plot, around $M_{\text{UV}} \sim -20$, is due to the EW probability distribution threshold between UV-bright and UV-faint galaxies (see Mason et al. 2018), and is discussed further in Section 3.1.

expectation value is defined as

$$\langle L_\alpha \rangle = \int_{L_{\min}}^{L_{\max}} L_\alpha \cdot P_{\text{norm}}(L_\alpha | M_{\text{UV}}) dL_\alpha, \quad (14)$$

$$P_{\text{norm}}(L_\alpha | M_{\text{UV}}) = \frac{P(L_\alpha | M_{\text{UV}})}{\int_{L_{\min}}^{L_{\max}} P(L_\alpha | M_{\text{UV}})}, \quad (15)$$

where we calculate the integrals over the range $10^{36} < L_\alpha < 10^{44.5} \text{ erg s}^{-1}$. This range (i.e., a range greater than zero) is chosen because we want to observe the typical $\langle L_\alpha \rangle$ – M_{UV} relation for $\text{Ly}\alpha$ emitters. We also want to ensure coverage of the $\text{Ly}\alpha$ luminosity values over the M_{UV} range $-24 \leq M_{\text{UV}} \leq -12$.

Figure 3 demonstrates that for UV-bright galaxies, $M_{\text{UV}} \lesssim -20$, we expect an average $\text{Ly}\alpha$ luminosity of $L_\alpha \sim 10^{42} - 10^{43.6} \text{ erg s}^{-1}$. For UV-faint galaxies we expect a lower typical $\text{Ly}\alpha$ luminosity of $L_\alpha \sim 10^{39} - 10^{41} \text{ erg s}^{-1}$. Here, we also show how $\langle L_\alpha \rangle$ compares for galaxies brighter or fainter than M_{UV}^* (where we use $M_{\text{UV}}^* = -20.9$ at $z = 6.0$ from Mason et al. 2015b).

Figure 3 shows a decrease in $\text{Ly}\alpha$ luminosity for a given M_{UV} as x_{HI} increases, as expected due to the reduced transmission in an increasingly neutral IGM (Mason et al. 2018). This effect is strongest for UV-faint galaxies, where the average $\text{Ly}\alpha$ luminosity decreases by a factor of ~ 10 as x_{HI} increases to 1. UV-bright galaxies do not show much decrease in $\text{Ly}\alpha$ luminosity at different x_{HI} . The more sizeable impact of reionization on UV-faint galaxies is because they typically exist in the outskirts of dense IGM environments. Thus, a more

neutral IGM shifts their $\text{Ly}\alpha$ luminosity toward even lower values.

The bump in the plot, around $M_{\text{UV}} \sim -20$, is due to the EW probability distribution threshold between UV-bright and UV-faint galaxies (Mason et al. 2018). We tested the importance of this bump by fixing the $P(\text{EW})$ distribution (in our case we tested at $P(\text{EW}|M_{\text{UV}}) = P(\text{EW}|M_{\text{UV}} = -17)$), which removes the bump. However, this drastically affected the $\text{Ly}\alpha$ LF model where it does not fit observations well on the bright end. This means that $P(\text{EW})$ must be shifted to lower EW values for galaxies brighter than $M_{\text{UV}} < -20$.

3.2. Evolution of the $\text{Ly}\alpha$ LF

We compare our model $\text{Ly}\alpha$ LF to observations at $z = 5.7, 6.6, 7.0$, and 7.3 . In Figure 4, we plot our $\text{Ly}\alpha$ LF models for a range of x_{HI} from a fully neutral to fully ionized IGM at a given redshift. We also plot observations by Ouchi et al. (2008), Ouchi et al. (2010), Shibuya et al. (2012), Konno et al. (2014), Santos et al. (2016), Ota et al. (2017), Konno et al. (2018), Itoh et al. (2018), Hu et al. (2019), and Taylor et al. (2020) for comparison. Note that we use the selection incompleteness uncorrected LFs by Hu et al. (2019) for the best comparison with other observations and our model, which is calibrated using data that do not account for this incompleteness. Our simple model reproduces the shape of the $\text{Ly}\alpha$ LF remarkably well. Note that our $\text{Ly}\alpha$ LF is slightly lower than the one observed by Santos et al. (2016). This mismatch between their $\text{Ly}\alpha$ LF and other works found in literature is known and discussed, e.g., in Taylor et al. (2020) and Hu et al. (2019).

We see that at $z = 5.7, 6.6$, and 7.0 the observations are fairly consistent with $x_{\text{HI}} \sim 0.15 - 0.36$, whereas at $z = 7.3$ the data are more consistent with $x_{\text{HI}} \sim 0.66 - 0.87$, suggesting an increasingly neutral IGM environment as redshift increases, consistent with other observations at $z \sim 7$ (e.g., Mason et al. 2018; Whitler et al. 2020; Mason et al. 2019; Hoag et al. 2019).

Our model predicts that there is not much decrease in number density at low neutral fractions, $x_{\text{HI}} \lesssim 0.4$, but the LF decreases more rapidly at higher neutral fractions. Based on Figure 3 the lack of evolution at $x_{\text{HI}} \lesssim 40\%$ can be explained by the fact that the bright end of the $\text{Ly}\alpha$ LF is dominated by UV-bright galaxies, which exist in over-dense regions of IGM that tend to reionize early (Mesinger & Furlanetto 2007; Mesinger 2016; Harikane et al. 2018). Thus, only in reionization’s earliest stages do these galaxies experience a significant reduction in transmission.

3.3. Evolution of Schechter Function Parameters for the $\text{Ly}\alpha$ LF

We fit Schechter parameters, α, L^*, ϕ^* , for our models using emcee (Foreman-Mackey et al. 2013) to predict how the shape of the $\text{Ly}\alpha$ LF evolves with redshift and neutral fraction. To compare with observations, we fit the LF over the luminosity range $42.5 < \log_{10} L_\alpha / \text{erg s}^{-1} < 44$. We fit the Schechter function to our $\text{Ly}\alpha$ LF models with all possible combinations of redshift and x_{HI} but point out that the resulting $\text{Ly}\alpha$ LF are not exact Schechter functions for realistic $\text{Ly}\alpha$ EW distributions (even if the input UV LF is)—our $\text{Ly}\alpha$ LFs are generally less steep at the bright end than a Schechter function. Further details about the fitting are provided in Appendix A.

In Figure 5, we plot the evolution of each parameter (where we show the median value from the fits) with respect to redshift and x_{HI} . We see that the parameters decrease overall as

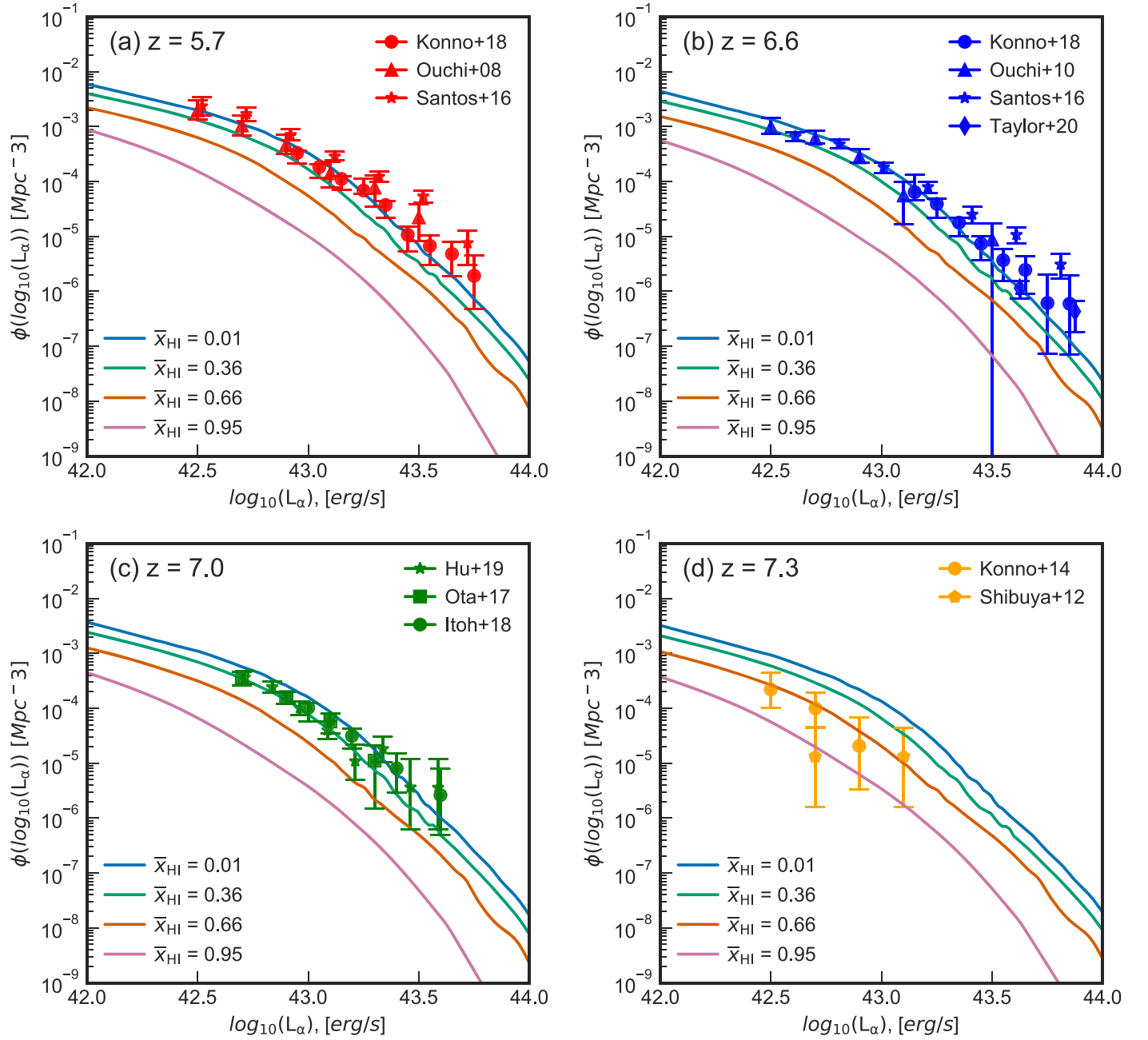


Figure 4. Our predictions for Ly α LF for $z = 5.7, 6.6, 7.0$, and 7.3 at $x_{\text{HI}} = 0.01\text{--}0.87$ (explained in Section 3.2). We also plot observations by Ouchi et al. (2008, 2010), Shibuya et al. (2012), Konno et al. (2014), Santos et al. (2016), Ota et al. (2017), Konno et al. (2018), Itoh et al. (2018), Hu et al. (2019), and Taylor et al. (2020) for comparison with our model. Each model line corresponds to a different neutral fraction. The Ly α LF model decreases and changes shape at each redshift as x_{HI} increases. By comparing the observations to our model, as redshift increases, an increasingly neutral IGM is favored.

the universe becomes more neutral due to Ly α photon attenuation and decrease with redshift because galaxies become fainter and rarer as redshift increases (as seen in the UV LF (Figure 2)).

The left panel of Figure 5 shows redshift versus α , which is the power-law slope for very low luminosities. At fixed x_{HI} , α decreases as redshift increases, within the slope range of approximately $-2.5 < \alpha < -1.8$, as expected due the hierarchical build-up of galaxies producing an increasingly steep faint-end slope of the UV LF with redshift (Mason et al. 2015b). The points plotted at each redshift show the impact of neutral hydrogen. α decreases significantly more due to the neutral gas than it does with redshift because Ly α attenuation affects faint

galaxies more and thus makes them fainter, forcing them further back into the Ly α LF.

The center panel of Figure 5 reveals that L^* decreases in the range $z = 5\text{--}7$, but increases sharply toward $z = 8$, and declines toward higher redshifts at fixed neutral fractions. This upturn is a consequence of the evolving shape of the UV LF due to dust attenuation at these redshifts in our model. In Mason et al. (2015b), there is an overlapping between $z = 6$ and 8 for the UV LF model around $M_{\text{UV}} = -23$, which corresponds to $L_\alpha = 10^{43.6} \text{ erg s}^{-1}$, also seen in observations (e.g., Bouwens et al. 2016, 2015). This overlapping is consistent with a reduction in dust obscuration, such that younger, brighter galaxies at higher redshifts contain less dust, and so, there is a

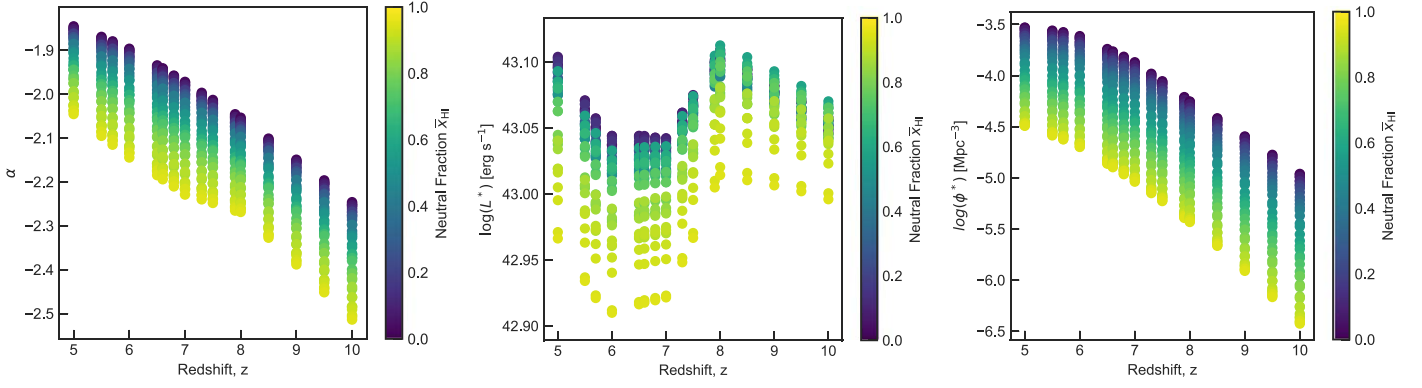


Figure 5. The evolution of the Schechter function parameters α , L^* , ϕ^* (left, center, right panels, respectively), as a function of redshift $z = 5$ – 10 with a step of $\Delta z = 0.5$. Models at different average neutral fractions, x_{HI} , are shown with different colors referenced on the adjacent color bar. Further details about the fitting procedure are explained in Section 3.3 and Appendix A. We find strong evolution of the Schechter function parameters with x_{HI} , in which each parameter decreases as the neutral fraction increases because Ly α photons become more attenuated.

possibility of observing more of them and shifting the LF models toward higher luminosities. As the neutral fraction increases at each redshift, the characteristic Ly α luminosity, L^* , decreases. This trend can be attributed to an increasing attenuation of Ly α photons from UV-bright galaxies as the neutral fraction increases.

The right panel of Figure 5 shows a decreasing number density of Ly α emitting galaxies as we look back to higher redshifts. For each redshift, as shown, assuming the IGM is ionized, more Ly α emitting galaxies are expected to be visible to us and thus the number density increases with decreasing redshift, compared to a neutral IGM. At higher redshifts and at a fixed neutral fraction, we see an overall decrease in number density of Ly α emitters—due to the overall reduction in the number of galaxies at high redshifts (as seen in the evolution of the UV LF, e.g., Bouwens et al. 2015, 2016; Mason et al. 2015b).

We did not compare our Schechter function parameters directly with observations as previous works used a fixed α to determine their best-fit Schechter function parameters (e.g., Konno et al. 2014, 2018; Ouchi et al. 2008, 2010; Itoh et al. 2018; Ota et al. 2017; Hu et al. 2019). As the Schechter function parameters are degenerate (see, e.g., the discussion in Herenz et al. 2019), it is difficult to compare with our model directly. Also note that our model for the Ly α LF is not well described by a Schechter fit—our model LFs are typically less steep at the bright end than a Schechter function’s exponential drop-off (see Figure 9). In our approach (Equation (16)) we do not expect the Ly α LF to be a Schechter form as the integral of the Schechter UV LF does not have a Schechter form, as discussed in Section 3.1 of Gronke et al. (2015). Physical reasons for an observed bright-end excess in the Ly α LF are discussed in Section 4.1 of Konno et al. (2018), including the contribution of AGN, large ionized bubbles around bright LAEs, and gravitational lensing.

3.4. Evolution of Ly α LD

The Ly α LD is the total energy emitted in Ly α by all galaxies obtained by integrating the LF:

$$\rho_\alpha(z, x_{\text{HI}}) = \int L_\alpha \phi(L_\alpha, z, x_{\text{HI}}) dL_\alpha, \quad (16)$$

where $\phi(L_\alpha, z, x_{\text{HI}})$ is our Ly α LF model number density. We generate $\rho_\alpha(z, x_{\text{HI}})$ from our model by integrating over our

luminosity grid $10^{42.4} \leq L_\alpha \leq 10^{44.5} \text{ erg s}^{-1}$ to compare with observations that use similar luminosity limits, as the LD is highly sensitive to the minimum luminosity, due to the power-law slope of the LF faint end.

Figure 6 shows the evolution of the LD along a range of redshifts, $z = 5$ – 10 , and the neutral fraction, x_{HI} , predicted by our model. The modeled LD decreases by a factor of ~ 10 as the universe becomes more neutral and declines overall as redshift increases. Observations from Konno et al. (2014), Konno et al. (2018), Hu et al. (2019), Itoh et al. (2018), and Ota et al. (2017) at $z = 5.7, 6.6, 7.0$, and 7.3 show a decrease in LD to higher redshifts. We compare our model with observations and see that the LD observations are consistent with a mostly ionized IGM at $z = 5.7, 6.6$, and 7.0 , and increase toward a more neutral IGM at $z = 7.3$. These observations, similar to the Ly α LF observations, are chosen based on their selection incompleteness being uncorrected further explained in Hu et al. (2019). We also chose to plot Ly α LD observations that were considered fiducial (some works also tested separate LD points at different α to compare with others).

3.5. The Evolution of the Neutral Fraction at $z > 6$

We perform a Bayesian inference for the neutral fraction based on our model, as explained in Section 2.4. We infer x_{HI} at $z = 6.6, 7.0$, and 7.3 by fitting our model to LF observations by Shibuya et al. (2012), Konno et al. (2014), Konno et al. (2018), Itoh et al. (2018), Ota et al. (2017), and Hu et al. (2019). We infer $x_{\text{HI}}(z = 6.6) = 0.08^{+0.08}_{-0.05}$, $x_{\text{HI}}(z = 7.0) = 0.28 \pm 0.05$ and $x_{\text{HI}}(z = 7.3) = 0.83^{+0.06}_{-0.07}$ (all errors are 1σ credible intervals). Appendix B shows the posterior distributions for x_{HI} at each redshift (Figure 10).

We also show the comparisons between the posterior distributions for the neutral fraction obtained using the Ly α LD observations (Konno et al. 2014; Ota et al. 2017; Konno et al. 2018; Itoh et al. 2018; Hu et al. 2019, see Section 3.4). As expected, we see larger uncertainties in the estimations of the neutral fraction from the Ly α LD data due to including fewer data points compared to the LFs. We find $x_{\text{HI}}(z = 6.6) = 0.22^{+0.12}_{-0.11}$, $x_{\text{HI}}(z = 7.0) = 0.25 \pm 0.08$, and $x_{\text{HI}}(z = 7.3) = 0.69^{+0.12}_{-0.11}$. Using the full LF data thus not only enables us to infer neutral fractions that are more robust to nonuniform Ly α transmission, but adds a statistical advantage over previous LD methods by reducing the

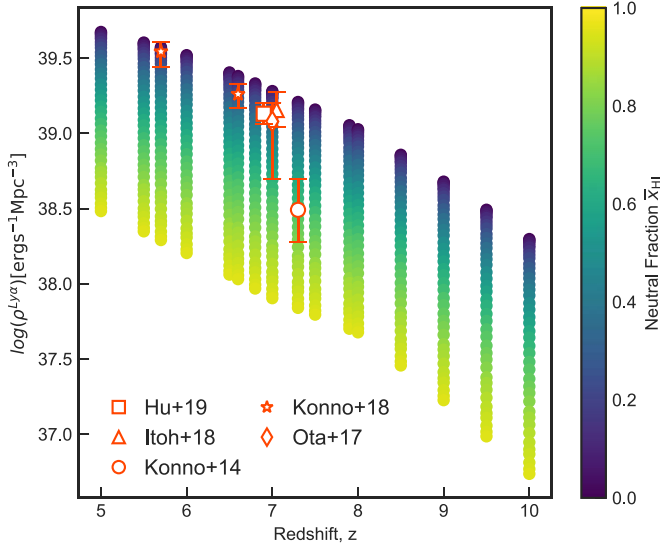


Figure 6. Evolution of the Ly α LD as a function of redshift and the IGM neutral fraction between $z = 5$ and 10. Observational data from Konno et al. (2018) (orange stars, $z = 5.7$ and 6.6), Hu et al. (2019) (orange squares, $z = 6.9$), Itoh et al. (2018) (orange triangles, $z = 7.0$), Ota et al. (2017) (orange diamonds, $z = 7.0$), and Konno et al. (2014) (orange circles, $z = 7.3$) show a clear drop in the overall Ly α LD as redshift increases. The LD model shows a decreasing trend as redshift increases and we can expect to see lower LD values as the neutral fraction increases at any redshift.

uncertainty on the neutral fraction (for further discussion, we refer the reader to Section 4.2).

Figure 7 shows our new constraints on reionization history along with other approaches to estimating the neutral fraction. Our results show clear upward trend in neutral fraction at higher redshifts, consistent with an IGM that reionizes fairly rapidly. Our measurement at $z = 6.6$ is consistent with previous upper limits on the neutral fraction at $z \leq 6.6$ (McGreer et al. 2015; Ouchi et al. 2010; Sobacchi & Mesinger 2015). Our measurement at $z = 7.0$ is consistent with inferences from the Ly α damping wing in the quasar ULAS J1120+0641 (Davies et al. 2018), but is lower than than constraints from the Ly α EW distribution in LBGs by Mason et al. (2018) and Whittler et al. (2020), though is still consistent within 2σ . Our measurement at $z = 7.3$ is consistent with other constraints at $z > 7$ (Hoag et al. 2019; Mason et al. 2019; Davies et al. 2018) though, like the other $z > 7$ constraints, is higher than the QSO damping wing measurements at $z = 7.5$ for the quasar ULAS J1342+0928 by Greig et al. (2019).

3.6. Predictions for the NGRST, Euclid, and JWST Surveys

The NGRST High Latitude Survey (HLS) and the Euclid Deep Field Survey (DFS) will both be particularly important surveys that will probe into higher redshifts and detect Ly α emission lines further into the Epoch of Reionization with wide-area slit-less spectroscopy. JWST will also be able to detect high-redshift Ly α with high sensitivity, albeit in smaller areas. Here we make predictions for potential Ly α LFs with these telescopes.

The Euclid DFS will cover a 40 deg² area at a 5σ flux limit of $\sim 8.6 \times 10^{-17}$ erg s⁻¹ cm⁻². It will cover $0.9 \leq \lambda_{\text{obs}} \leq 1.3 \mu\text{m}$ corresponding to a redshift range for Ly α of $6 \leq z \leq 10$ (e.g., Laureijs et al. 2012; Bagley et al. 2017). The NGRST HLS will cover $1.00 \leq \lambda_{\text{obs}} \leq 1.95 \mu\text{m}$ corresponding to a redshift range for Ly α of $8 \leq z \leq 15$, and survey a 2200 deg²

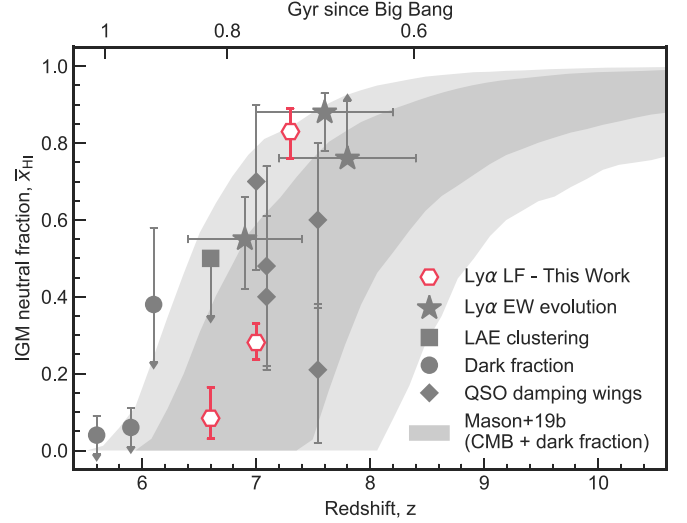


Figure 7. IGM neutral fraction of hydrogen as a function of redshift updated from Mason et al. (2018). Reionization history plot with this work corresponding to the Ly α LF given a 1σ uncertainty (red hexagons). Constraints derived from observations of previous estimates from the fraction of LBGs emitting Ly α are plotted (star; Mason et al. 2018, 2019; Whittler et al. 2020; Hoag et al. 2019); the clustering of Ly α emitting galaxies (square; Ouchi et al. 2010; Sobacchi & Mesinger 2015); Ly α and Ly β forest dark fraction (circle; McGreer et al. 2015); and QSO damping wings (diamond; Greig & Mesinger 2017; Davies et al. 2018; Greig et al. 2019; Wang et al. 2020). The shaded regions of the reionization plot show the corresponding 1σ and 2σ uncertainty coverage consistent with Planck Collaboration et al. (2016) τ and dark fraction (Mason et al. 2019).

area at a 5σ flux limit of $\sim 7.1 \times 10^{-17}$ erg s⁻¹ cm⁻² (e.g., Ryan et al. 2019; Spergel et al. 2013). JWST's Near Infrared Imager and Slitless Spectrograph (NIRISS) will cover $0.7 \leq \lambda_{\text{obs}} \leq 5.0 \mu\text{m}$, capable of detecting Ly α at $z \gtrsim 5$. While there is no dedicated wide-area survey with NIRISS, we investigate a mock pure-parallel survey of 50 pointings (~ 240 arcmin²) with a 5σ flux limit of $\sim 5.0 \times 10^{-18}$ erg s⁻¹ cm⁻², assuming 2 hr exposures with the F115W filter.

We make predictions for these surveys in Figure 8. We plot our model Ly α LF and the approximate median neutral fraction value based the reionization history allowed by the cosmic microwave background (CMB) optical depth and dark pixel fraction at each redshift (Mason et al. 2019) between $6 < z < 10$ (shown as the gray shaded region in Figure 7). We see that these surveys will detect luminous Ly α emitters at higher redshifts. We predict the NGRST HLS will be able to discover galaxies $L_{\alpha} > 10^{43.76}$ erg s⁻¹ at redshifts up to $z = 10$. The Euclid DFS will be able to detect bright galaxies at $L_{\alpha} > 10^{43.84}$ erg s⁻¹ but only up to $z \sim 8$. Using the JWST mock pure-parallel survey, we estimate it be able to detect bright galaxies at $L_{\alpha} > 10^{42.61}$ erg s⁻¹ up to $z \sim 9-10$.

We note that the predicted number counts will likely be higher than shown in Figure 8 due to gravitational lensing magnification bias, which can increase the observed number of galaxies at the bright end of the LF in flux-limited surveys (Wyithe et al. 2011; Mason et al. 2015a; Marchetti et al. 2017).

4. Discussion

In this section, we discuss uncertainties that affect our Ly α LF model (Section 4.1), a comparison with previous work that attempted to constrain reionization from Ly α LFs (Section 4.2), and an explanation of our Ly α luminosity distributions for both

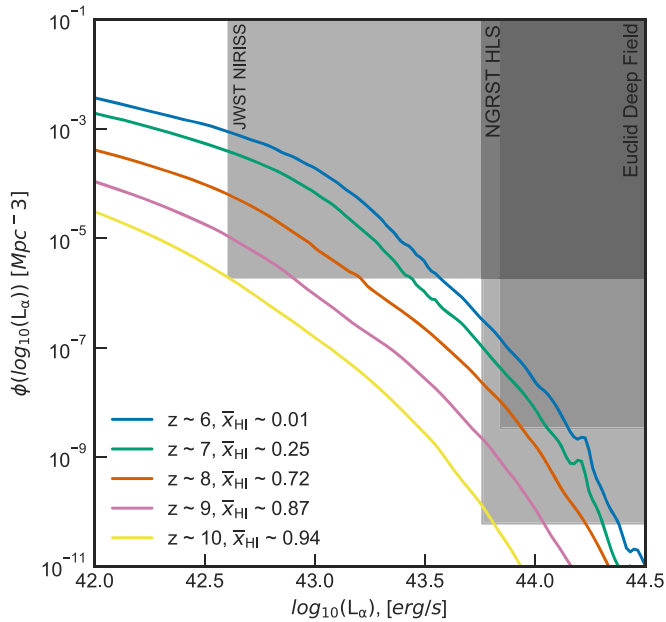


Figure 8. $\text{Ly}\alpha$ LF model at redshifts $z = 6$ – 10 and their corresponding median neutral fraction values. The shaded boxes represent the survey depth coverage for the NGRST HLS (a 5σ flux limit of $\sim 7.1 \times 10^{-17} \text{ erg s}^{-1} \text{ cm}^{-2}$ and a redshift range of $8 \leq z \leq 15$ (e.g., Ryan et al. 2019; Spergel et al. 2013), the Euclid DFS (a 5σ flux limit of $\sim 8.6 \times 10^{-17} \text{ erg s}^{-1} \text{ cm}^{-2}$ and a redshift range of $6 \leq z \leq 10$ (e.g., Laureijs et al. 2012; Bagley et al. 2017), and the JWST NIRISS mock pure-parallel survey (a 5σ flux limit of $\sim 5.0 \times 10^{-18} \text{ erg s}^{-1} \text{ cm}^{-2}$ and a redshift range of $z \gtrsim 5$). We calculate the luminosity limits and depths for the NGRST HLS, Euclid DFS, and JWST NIRISS mock pure-parallel survey at a median redshift value of $z = 8$.

$\text{Ly}\alpha$ and UV-selected galaxies and their effect on the normalization factor (Section 4.3).

4.1. Modeling Caveats

In building our model, we make several assumptions that can affect the results, which are summarized here. These assumptions are also described by Mason et al. (2018) and Whitley et al. (2020), and we refer the reader there for additional details. First, we assume that the intrinsic *emitted* $\text{Ly}\alpha$ luminosity distribution does not evolve with redshift (only M_{UV}) and is the same as the observed $\text{Ly}\alpha$ luminosity distribution at $z \sim 6$ (as modeled from the EW distribution by Mason et al. 2018), and that only evolution in the *observed* luminosity distribution is due to reionization alone. However, we should expect some evolution in the $\text{Ly}\alpha$ luminosity distribution with redshift, as galaxy properties evolve. Physically, we could expect galaxies to have higher luminosities as redshift increases, due to, e.g., lower dust attenuation (Hayes et al. 2011), which leads to a steepening of the $\text{Ly}\alpha$ LF with redshift (Gronke et al. 2015; Dressler et al. 2015). In that case, more significant absorption by the IGM would be required to explain the observed $\text{Ly}\alpha$ LFs and we would thus infer a higher neutral fraction. Alternatively, a decrease in outflow velocities possibly associated with a decreasing specific star formation rate could lower $\text{Ly}\alpha$ escape from galaxies, decreasing the emitted luminosity (Hassan & Gronke 2021), in which case a lower neutral fraction would be inferred.

We also assume that $\text{Ly}\alpha$ visibility evolution between $z = 6$ and 7 is due only to the evolution of the $\text{Ly}\alpha$ damping wing optical depth (e.g., Miralda-Escudé 1998), due to the diffuse neutral IGM. We do not model redshift evolution of the $\text{Ly}\alpha$

transmission in the ionized IGM or circumgalactic medium (CGM) at fixed halo mass (e.g., Laursen et al. 2011; Weinberger et al. 2018). The amount of transmission due to these components is determined by the $\text{Ly}\alpha$ line shape. If the $\text{Ly}\alpha$ line velocity offset from systemic decreases with redshift at fixed halo mass, this would decrease the $\text{Ly}\alpha$ transmission throughout the ionized IGM and CGM (Dijkstra et al. 2011; Choudhury et al. 2015) and reduce the need for a highly neutral IGM. A full exploration of the degeneracies and systematic uncertainties due to the $\text{Ly}\alpha$ emission model is left to future work.

4.2. Comparison with Previous Work

In this work we directly compare measurements of the $\text{Ly}\alpha$ LF to our model. Previous works, e.g., Ouchi et al. (2010), Zheng et al. (2017), Konno et al. (2014), Konno et al. (2018), Inoue et al. (2018), and Hu et al. (2019), estimate the neutral fraction by evaluating the $\text{Ly}\alpha$ luminosity density. While this provides a reasonable first-order estimate, this method can be difficult to interpret as it relies on models and observations using the same luminosity limit in the luminosity density integral, and it collapses any valuable information that is obtained in the evolving *shape* of the $\text{Ly}\alpha$ LF (including increasing the statistical uncertainty on x_{HI} by reducing the number of data points—see Appendix B). As demonstrated in Section 3.3, the $\text{Ly}\alpha$ shape does evolve.

Furthermore, these works estimate the neutral fraction based on the assumption that the transmission fraction, T_{IGM} , is constant for all galaxies. However, as shown by, e.g., Mason et al. (2018) and Whitley et al. (2020) it is a broad distribution and depends on galaxy properties, through their large scale structure environment and the internal kinematics that sets the $\text{Ly}\alpha$ line shape. If the transmission fraction varies with $\text{Ly}\alpha$ or UV luminosity, the common method of calculating $\text{Ly}\alpha$ transmission by taking the ratio of the $\text{Ly}\alpha$ luminosity density at different redshifts is invalid, thus our work enables a more robust estimate of x_{HI} from the $\text{Ly}\alpha$ LFs. Many of these works compare with simulations by McQuinn et al. (2007), which do model the impact of inhomogeneous reionization on the $\text{Ly}\alpha$ LF but take a more simplistic approach to modeling $\text{Ly}\alpha$ luminosity: each galaxy has a $\text{Ly}\alpha$ luminosity proportional to its mass. In our work, we use the EW probability distribution from Mason et al. (2015b) to take into account that galaxies have a range of $\text{Ly}\alpha$ EW at fixed UV magnitude. Our approach is thus more similar to that of Jensen et al. (2013), who model the $\text{Ly}\alpha$ luminosity probability distribution as a function of halo mass. However, Jensen et al. (2013) model the $\text{Ly}\alpha$ luminosity and EW distributions independently, whereas we have shown the $\text{Ly}\alpha$ LF can be self-consistently described by the same $\text{Ly}\alpha$ EW distribution that describes LBGs.

Finally, our semi-analytic model provides flexibility over approaches that model radiative transfer in N-body simulations (e.g., Dayal et al. 2011; Jensen et al. 2013; Hutter et al. 2014; Inoue et al. 2018) or sophisticated hydrodynamical simulations (e.g., Dayal et al. 2011; Weinberger et al. 2019) by keeping the IGM neutral fraction and redshift as free parameters, rather than assuming a fixed reionization history. Using this new model for the $\text{Ly}\alpha$ LF, we can separate redshift and the neutral fraction, fixing either parameter if needed, and see how observations compare to our model.

4.3. Reconciling the Ly α Luminosity Distributions for Ly α and UV-selected Galaxies

As described in Section 2.3, a normalization factor, F , is introduced to the Ly α LF to account for any mismatch in the number density of LAEs (Dijkstra & Wyithe 2012). If the Ly α luminosity distribution model accurately describes the LBG population observed in the UV LF, we expect $F = 1$. We find $F = 0.974$ in our model, which is considerably higher than previous work focusing on the Ly α LF at lower redshifts, which found $F \sim 0.5$ (Dijkstra & Wyithe 2012; Gronke et al. 2015).

The key difference compared to this previous work that leads to our model successfully reproducing the Ly α LF without the need for additional normalization is due to the EW distribution we employed. While we, as well as the previous work, include non-emitters in the model, the EW distribution used by Dijkstra & Wyithe (2012), Gronke et al. (2015) (calibrated to the measurements of Shapley et al. 2003; Stark et al. 2010, 2011, at $z \sim 3-6$) shows an increasing probability of Ly α emission for lower UV brightness galaxies, leading to a Ly α emitter (EW > 0 Å) fraction of unity for $M_{UV} \gtrsim -19$. The EW distribution we used caps this emitter fraction at 65% (our function $A(M_{UV})$ in Section 2.1.1).

Which parameterization of the EW distribution is most appropriate is still up for debate (see, e.g., the detailed discussion by Oyarzún et al. 2017, who study more complex distributions also dependent on the stellar mass and the UV slope). The recent study of Caruana et al. (2018) supports our non-emitter fraction, as they find a fraction of $\sim 0.5 \pm 0.15$ galaxies with EW > 0 Å at $3 < z < 6$ in Hubble Space Telescope (HST) continuum selected galaxies for within the Multi Unit Spectroscopic Explorer (MUSE) wide field (Herenz et al. 2017; Urrutia et al. 2019) is present. However, Caruana et al. (2018) also find a non-evolution of this fraction with UV magnitude (in contrast with previous models) as well as typically lower Ly α fractions for larger EW cuts (e.g., the value for $W > 50$ Å seems to be in slight tension with measurements by Stark et al. (2010), who find $\approx 45\% \pm 10\%$ of galaxies have Ly α EW > 55 Å and a strong anticorrelation with UV brightness).

Another factor to consider when comparing $z \lesssim 3$ and $z \gtrsim 5$ EW distributions is the impact of the IGM on the Ly α line even at $z \sim 5-6$. In fact, it is has been suggested by Weinberger et al. (2019) that F could stem from this effect but note that Dijkstra & Wyithe (2012) and Gronke et al. (2015) compare their modeled Ly α LFs at $z \sim 3$ to data by Ouchi et al. (2008); Gronwall et al. (2007) and Rauch et al. (2008), respectively, and still require $F \sim 0.5$ at this low z .

Future observational studies will constrain the Ly α EW distribution further both as a function of redshift and UV magnitude, and thus can quantify the fraction of non-emitters for UV-faint galaxies. We have shown that a constant non-emitter fraction of $\sim 35\%$ for $M_{UV} \lesssim -19$ makes the fudge factor $F \sim 0.5$ obsolete, which indicates that such a *cutoff* exists in reality.

5. Conclusions

We have developed a model for the Ly α LF during reionization, and compared it with observations at specific redshifts to estimate the evolution of the neutral fraction. Our model can be extended to predict the evolution of the Ly α LF with neutral fraction at even higher redshifts, deeper in the era of reionization. Our model takes into account inhomogeneous

reionization, enabling us to understand the impact of galaxy environment on the Ly α LF.

Our conclusions are as follows:

1. By combining previously established models for the UV LF and the Ly α EW distribution for UV-selected galaxies, we successfully reproduce the observed $z = 5.7$ Ly α LF (derived from Ly α -selected galaxies).
2. Our model predicts a decline in the Ly α LF as the neutral fraction increases. For $x_{\text{H I}} \lesssim 0.4$, the Ly α LF models exhibit relatively little decrease in number density; however, at higher neutral fractions we see a significant drop in number density.
3. We predict that the average Ly α luminosity for a LBG of a given UV magnitude decreases as the neutral fraction increases. We find there is only a moderate decrease in Ly α luminosity for UV-bright galaxies at increasing $x_{\text{H I}}$ (factor of ~ 2 from a fully ionized to fully neutral IGM) because they typically exist in dense regions of the universe that reionize early, allowing large amounts of Ly α photons to be transmitted. For UV-faint galaxies, which are typically found in neutral IGM regions, we see a decrease in Ly α luminosity by a factor of ~ 10 with the neutral fraction.
4. We find strong evolution of the Schechter function parameters with $x_{\text{H I}}$, demonstrating the LF shape changes. The faint-end slope α , number density ϕ^* and the characteristic luminosity L^* all generally decrease with increasing neutral fraction. These decreases in the Schechter function parameters with increasing $x_{\text{H I}}$ can be explained by a reduction in Ly α luminosity from all galaxies, with the faintest galaxies experiencing the most significant decline in transmission, which shifts the faint-end slope to steeper values.
5. The Ly α luminosity density decreases overall as the universe becomes more neutral, as shown by previous work.
6. We perform a Bayesian inference of the IGM neutral fraction given observations using our model. We infer an IGM neutral fraction at $z = 6.6$ of $x_{\text{H I}} = 0.08^{+0.08}_{-0.05}$, rising to $x_{\text{H I}} = 0.28 \pm 0.05$ for $z = 7.0$ and $x_{\text{H I}} = 0.83^{+0.06}_{-0.07}$ for $z = 7.3$, providing further evidence for a late and fairly rapid reionization.
7. Using our Ly α LF model with a fiducial reionization history, we predict the NGRST HLS will be able to discover bright galaxies with $L_{\alpha} > 10^{43.76}$ erg s $^{-1}$ at redshifts up to $z = 10$. Euclid DFS will be able to detect bright galaxies at $L_{\alpha} > 10^{43.84}$ erg s $^{-1}$ but only up to $z \sim 8$. Using a JWST mock pure-parallel survey, we estimate it will be able to detect galaxies at $L_{\alpha} > 10^{42.61}$ erg s $^{-1}$ up to $z \sim 9-10$.

Constraining the evolving shape of the Ly α LF as a function of redshift provides an important tool to estimate the evolving neutral fraction during reionization. Understanding the timeline of reionization and the properties of galaxies that existed as a function of redshift, and how they are impacted by neutral gas, can ultimately be used to infer properties of the first stars and galaxies that initialized reionization.

The authors thank Masami Ouchi, Weida Hu, Kazuaki Ota, Akio Inoue, Yoshiaki Ono, and Takatoshi Shibuya for sharing the Ly α LF observations from Ouchi et al. (2008), Ouchi et al. (2010),

Hu et al. (2019), Ota et al. (2017), Itoh et al. (2018), and Shibuya et al. (2012). A.M.M. thanks Matthew Ashby and Jonathan McDowell for their support throughout the SAO REU program and their feedback when revising early drafts of this paper.

The SAO REU program is funded in part by the National Science Foundation REU and Department of Defense ASSURE programs under NSF grant No. AST-1852268, and by the Smithsonian Institution. C.A.M. acknowledges support by NASA Headquarters through the NASA Hubble Fellowship grant HST-HF2-51413.001-A awarded by the Space Telescope Science Institute, which is operated by the Association of Universities for Research in Astronomy, Inc., for NASA, under contract NAS5-26555. C.S. and S.B. acknowledge the support from Jet Propulsion Laboratory under the grant award RSA 1646027. M.G. was supported by NASA through the NASA Hubble Fellowship grant HST-HF2-51409 and acknowledges support from HST grants HST-GO-15643.017-A and HST-AR15039.003-A, and XSEDE grant TG-AST180036.

Software: IPython (Pérez & Granger 2007), matplotlib (Hunter 2007), NumPy (Van Der Walt et al. 2011), SciPy (Oliphant 2007), Astropy (Robitaille et al. 2013), emcee (Foreman-Mackey et al. 2013).

Appendix A

Example of Fitting Schechter Function Parameters

Figure 9 shows examples of outputs for the best-fit Schechter function parameters for $z = 5.7$ and $x_{\text{H}} = 0.01$ as described in

Section 3.3. We perform a Bayesian inference (Equation (11)) to obtain the parameters, using the likelihood

$$P(\phi | \alpha, L_*, \phi_*) \propto \prod_i \exp \times [-(\ln \phi_{\text{mod}}(L_i) - \ln \phi_{\text{Sch}}(L_i, \alpha, L_*, \phi_*))^2], \quad (\text{A1})$$

where $\phi_{\text{mod}}(L_i)$ are our model Ly α LFs at luminosity values L_i , and $\phi_{\text{Sch}}(L_i, \alpha, L_*, \phi_*)$ is the Schechter function (Equation (1)). We perform the inference using *emcee* (Foreman-Mackey et al. 2013).

For all Schechter function fits, we restrict the fit to the luminosity range $41.0 < \log_{10} L_\alpha < 44.0 \text{ erg s}^{-1}$, and use the following uniform priors for the Bayesian inference: $-4 < \alpha < 0$, $40 < \log_{10} L_* < 44$ and $-10 < \log_{10} \phi_* < -2$. Example posteriors and fitted LFs are shown in Figure 9. We explored a variety of luminosity ranges for the fitting and note that the absolute values of the recovered Schechter parameters are quite sensitive to the fitted luminosity range; however, the trends in redshift and neutral fraction are consistent across the luminosity ranges, as long as $< L_*$ luminosities were included. Our model LFs have $L_* \sim 10^{43} \text{ erg s}^{-1}$, comparable to the luminosity limits of $z \gtrsim 7$ surveys (e.g., Ota et al. 2017; Hu et al. 2019), demonstrating the importance of deep LAE surveys to obtain accurate fits to the observed LFs. In our analysis in Section 3.3 we use the median values of the Schechter function parameters obtained from the posteriors. Note that our model for the Ly α LF is not well described by a Schechter fit—we see a shallower bright-end drop-off.

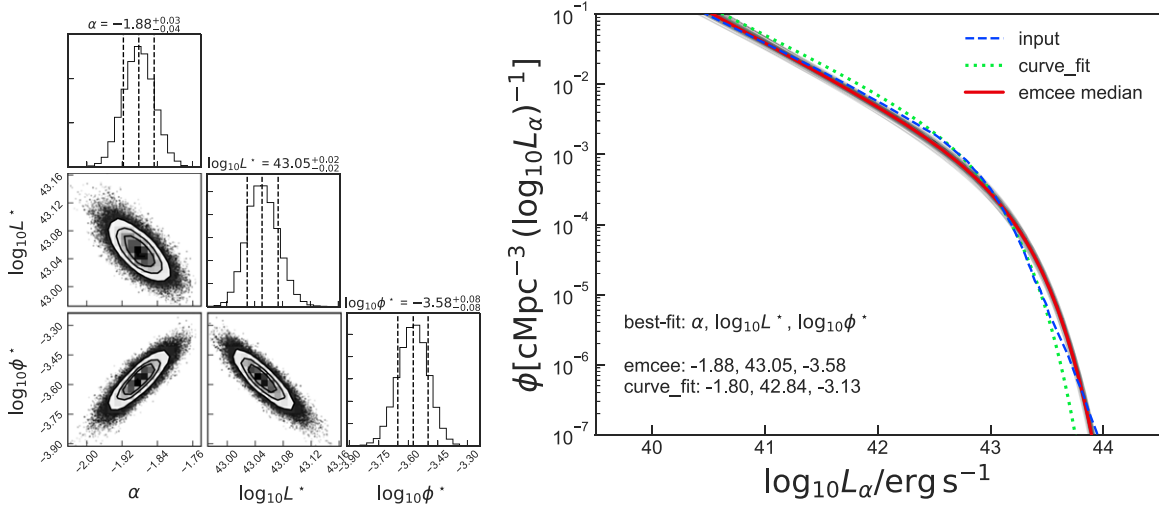


Figure 9. (Left) Posterior probability distributions for Schechter function parameters fit to our Ly α LF model at $z = 5.7$ and $x_{\text{H}} = 0.01$. (Right) Our Ly α LF model at $z = 5.7$ and $x_{\text{H}} = 0.01$ (blue dashed line) compared with the best-fit Schechter functions. Thin black solid lines show Schechter LFs with parameters from 100 draws from the posterior distribution. The Schechter LF obtained from the median of the posteriors is shown as the red solid line. We also plot the Schechter fit obtained using SciPy *curve_fit* for comparison (green dotted line). We use the median values of the Schechter function parameters for our analysis.

Appendix B

Inference of the Neutral Fraction, x_{HI} at $z = 6.6, 7.0$, and 7.3

To infer the neutral fraction we calculate a posterior distribution for $z = 6.6, 7.0$, and 7.3 . The posterior, defined in

Section 2.4, is normalized and plotted against neutral fraction values x_{HI} . To determine the 68% and 95% confidence intervals, we interpolate the inverse cumulative distribution function to find the neutral fraction value that falls at a given confidence interval value. Figure 10 shows the x_{HI} posterior at

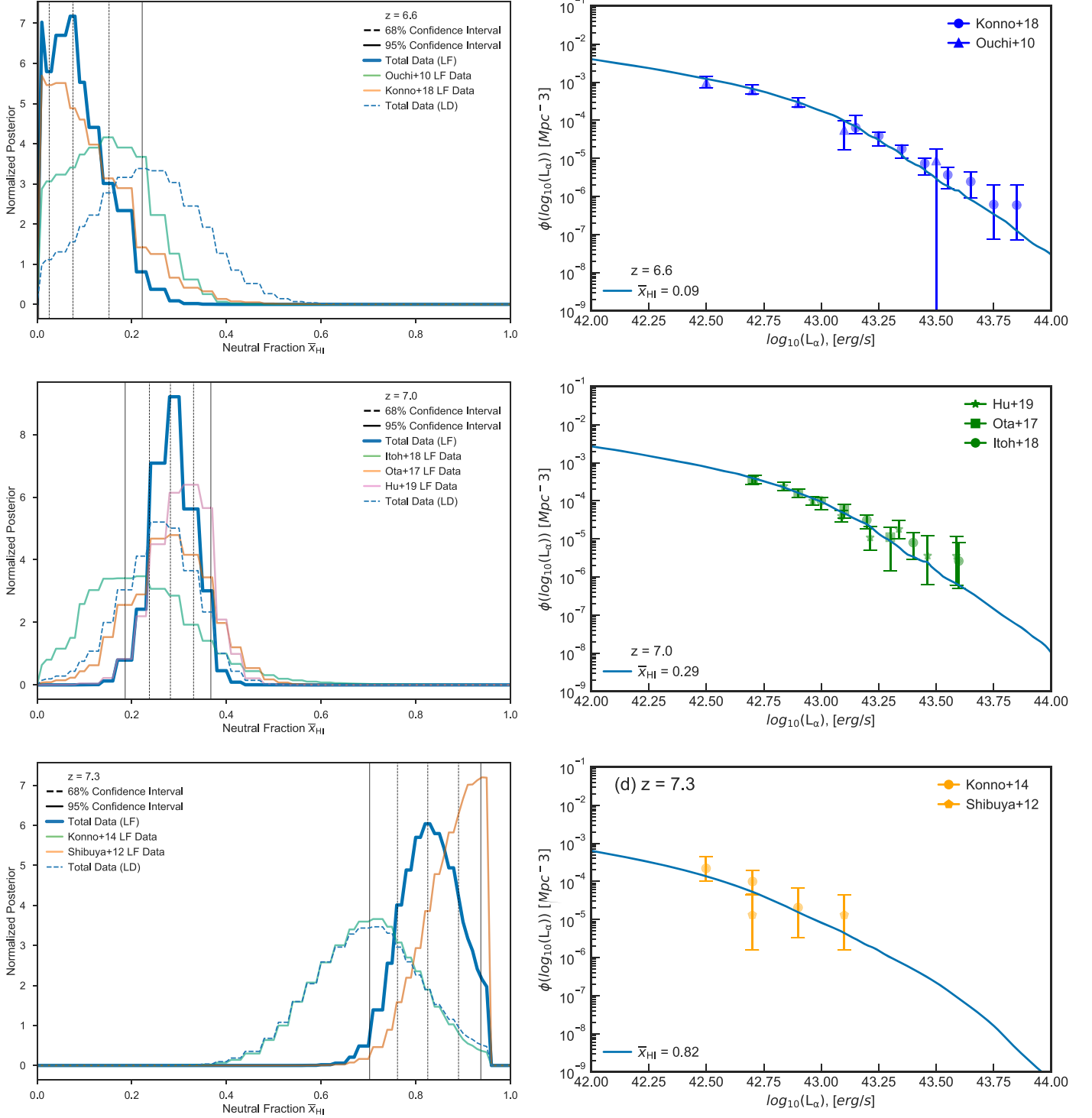


Figure 10. (Left) Neutral hydrogen fraction vs. the normalized posterior distribution $P(x_{\text{HI}} | \phi_{\text{obs}}, z)$ (see Section 2.4) for each redshift. The thick blue lines in each posterior plot show the total posterior distributions at each redshift alongside the individual posterior distributions for each data set (shown in either green, orange, or pink thin lines). The blue dashed lines correspond to total Ly α LD posterior distributions. The black dashed lines show the 68% or 1σ confidence interval where the upper, lower, and median limits are defined. The black solid lines show the upper and lower limits for the 95% or 2σ confidence interval. For redshifts $z = 6.6, 7.0$, and 7.3 , our median neutral fraction values (mid-dashed line on the left figures) is estimated to be $x_{\text{HI}}(z = 6.6) = 0.08$, $x_{\text{HI}}(z = 7.0) = 0.28$, and $x_{\text{HI}}(z = 7.3) = 0.83$. If we compare our total data posteriors, the Ly α LD posterior distribution has median neutral fraction values of $x_{\text{HI}}(z = 6.6) = 0.22$, $x_{\text{HI}}(z = 7.0) = 0.25$, and $x_{\text{HI}}(z = 7.3) = 0.69$. In Figure 7, we plot the median and 68% confidence interval values. (Right) We show the corresponding Ly α LF plot at that redshift and median neutral fraction value to verify our fit.

each redshift for both Ly α LF data and Ly α LD data, along with the confidence intervals. We also compare the Ly α LF models at the median x_{H} values to the data to verify our inferred values.

To verify advantages the Ly α LF may have over the Ly α LD in estimating the median neutral fraction, we establish the x_{H} posterior using the Ly α LD data. We expect larger uncertainties in the neutral fraction using only the LD data—the errors should roughly increase by \sqrt{N} , where N is the ratio of the number of individual data points with the two methods. Also note, some observations do not have Ly α LD data that can be included in the estimation of the neutral fraction (e.g., Ouchi et al. 2010; Shibuya et al. 2012) and thus also affect the results.

ORCID iDs

Alexa M. Morales  <https://orcid.org/0000-0003-4965-0402>
Charlotte A. Mason  <https://orcid.org/0000-0002-3407-1785>
Max Gronke  <https://orcid.org/0000-0003-2491-060X>
Francesco Haardt  <https://orcid.org/0000-0003-3291-3704>
Claudia Scarlata  <https://orcid.org/0000-0002-9136-8876>

References

- Ando, M., Ohta, K., Iwata, I., et al. 2006, *ApJL*, **645**, L9
Atek, H., Richard, J., Jauzac, M., et al. 2015, *ApJ*, **814**, 69
Bagley, M. B., Scarlata, C., Henry, A., et al. 2017, *ApJ*, **837**, 11
Bañados, E., Venemans, B. P., Mazzucchelli, C., et al. 2018, *Natur*, **553**, 473
Barkana, R., & Loeb, A. 2007, *RPPh*, **70**, 627
Bouwens, R. J., Illingworth, G. D., Oesch, P. A., et al. 2014, *ApJ*, **793**, 115
Bouwens, R. J., Illingworth, G. D., Oesch, P. A., et al. 2015, *ApJ*, **803**, 34
Bouwens, R. J., Oesch, P. A., Labbé, I., et al. 2016, *ApJ*, **830**, 67
Bowler, R. A. A., Dunlop, J. S., McLure, R. J., et al. 2015, *MNRAS*, **452**, 1817
Caruana, J., Wisotzki, L., Herenz, E. C., et al. 2018, *MNRAS*, **473**, 30
Choudhury, T. R., Puchwein, E., Haehnelt, M. G., & Bolton, J. S. 2015, *MNRAS*, **452**, 261
Ciardi, B., Stoehr, F., & White, S. D. M. 2003, *MNRAS*, **343**, 1101
Clément, B., Cuby, J. G., Courbin, F., et al. 2012, *A&A*, **538**, A66
Dahlen, T., Mobasher, B., Somerville, R. S., et al. 2005, *ApJ*, **631**, 126
Davies, F. B., Hennawi, J. F., Bañados, E., et al. 2018, *ApJ*, **864**, 142
Dayal, P., & Ferrara, A. 2018, *PhR*, **780**, 1
Dayal, P., Maselli, A., & Ferrara, A. 2011, *MNRAS*, **410**, 830
De Barros, S., Pentericci, L., Vanzella, E., et al. 2017, *A&A*, **608**, A123
Dijkstra, M., Mesinger, A., & Wyithe, J. S. B. 2011, *MNRAS*, **414**, 2139
Dijkstra, M., & Wyithe, J. S. B. 2012, *MNRAS*, **419**, 3181
Dressler, A., Henry, A., Martin, C. L., et al. 2015, *ApJ*, **806**, 19
Fan, X., Carilli, C., & Keating, B. 2006, *ARA&A*, **44**, 415
Finkelstein, S. L., D'Aloisio, A., Paardekooper, J. -P., et al. 2019, *ApJ*, **879**, 36
Finkelstein, S. L., Ryan, R. E. J., Papovich, C., et al. 2015, *ApJ*, **810**, 71
Foreman-Mackey, D., Hogg, D. W., Lang, D., & Goodman, J. 2013, *PASP*, **125**, 306
Furlanetto, S. R., & Oh, S. P. 2005, *MNRAS*, **363**, 1031
Gillet, N. J. F., Mesinger, A., & Park, J. 2020, *MNRAS*, **491**, 1980
Greig, B., & Mesinger, A. 2017, *MNRAS*, **465**, 4838
Greig, B., Mesinger, A., & Bañados, E. 2019, *MNRAS*, **484**, 5094
Greig, B., Mesinger, A., Haiman, Z., & Simcoe, R. A. 2017, *MNRAS*, **466**, 4239
Gronke, M., Dijkstra, M., Trenti, M., & Wyithe, S. 2015, *MNRAS*, **449**, 1284
Gronwall, C., Ciardullo, R., Hickey, T., et al. 2007, *ApJ*, **667**, 79
Harikane, Y., Ouchi, M., Ono, Y., et al. 2018, *PASJ*, **70**, S11
Hashimoto, T., Garel, T., Guiderdoni, B., et al. 2017, *A&A*, **608**, A10
Hassan, S., & Gronke, M. 2021, *ApJ*, **908**, 219
Hayes, M., Schaerer, D., Östlin, G., et al. 2011, *ApJ*, **730**, 8
Herenz, E. C., Urrutia, T., Wisotzki, L., et al. 2017, *A&A*, **606**, A12
Herenz, E. C., Wisotzki, L., Saust, R., et al. 2019, *A&A*, **621**, A107
Hibon, P., Cuby, J. G., Willis, J., et al. 2010, *A&A*, **515**, A97
Hoag, A., Bradač, M., Huang, K., et al. 2019, *ApJ*, **878**, 12
Hu, W., Wang, J., Zheng, Z. Y., et al. 2019, *ApJ*, **886**, 90
Hunter, J. D. 2007, *CSE*, **9**, 99
Hutter, A., Dayal, P., Partl, A. M., & Müller, V. 2014, *MNRAS*, **441**, 2861
Inoue, A. K., Hasegawa, K., Ishiyama, T., et al. 2018, *PASJ*, **70**, 55
Itoh, R., Ouchi, M., Zhang, H., et al. 2018, *ApJ*, **867**, 46
Jensen, H., Laursen, P., Mellema, G., et al. 2013, *MNRAS*, **428**, 1366
Jung, I., Finkelstein, S. L., Dickinson, M., et al. 2020, *ApJ*, **904**, 144
Jung, I., Finkelstein, S. L., Livermore, R. C., et al. 2018, *ApJ*, **864**, 103
Kelly, B. C., Fan, X., & Vestergaard, M. 2008, *ApJ*, **682**, 874
Konno, A., Ouchi, M., Nakajima, K., et al. 2016, *ApJ*, **823**, 20
Konno, A., Ouchi, M., Ono, Y., et al. 2014, *ApJ*, **797**, 16
Konno, A., Ouchi, M., Shibuya, T., et al. 2018, *PASJ*, **70**, S16
Krug, H. B., Veilleux, S., Tilvi, V., et al. 2012, *ApJ*, **745**, 122
Larson, R. L., Finkelstein, S. L., Pirzkal, N., et al. 2018, *ApJ*, **858**, 94
Laureijs, R., Gondoin, P., Duvet, L., et al. 2012, *Proc. SPIE*, **8442**, 84420T
Laursen, P., Sommer-Larsen, J., & Razoumov, A. O. 2011, *ApJ*, **728**, 52
Malhotra, S., & Rhoads, J. E. 2004, *ApJL*, **617**, L5
Marchetti, L., Serjeant, S., & Vaccari, M. 2017, *MNRAS*, **470**, 5007
Mason, C. A., Fontana, A., Treu, T., et al. 2019, *MNRAS*, **485**, 3947
Mason, C. A., Trenti, M., Treu, T., et al. 2015a, *ApJ*, **805**, 79
Mason, C. A., Trenti, M., & Treu, T. 2015b, *ApJ*, **813**, 21
Mason, C. A., Treu, T., Dijkstra, M., et al. 2018, *ApJ*, **856**, 2
Matthee, J. J. A., Sobral, D., Swinbank, A. M., et al. 2014, *MNRAS*, **440**, 2375
McGreer, I. D., Mesinger, A., & D'Odorico, V. 2015, *MNRAS*, **447**, 499
McQuinn, M., Hernquist, L., Zaldarriaga, M., & Dutta, S. 2007, *MNRAS*, **381**, 75
Mesinger, A. 2016, Understanding the Epoch of Cosmic Reionization: Challenges and Progress, Vol. 423 (Cham: Springer International Publishing)
Mesinger, A., Aykutalp, A., Vanzella, E., et al. 2014, *MNRAS*, **446**, 566
Mesinger, A., & Furlanetto, S. 2007, *ApJ*, **669**, 663
Miralda-Escudé, J. 1998, *ApJ*, **501**, 15
Miralda-Escudé, J., Haehnelt, M., & Rees, M. J. 2000, *ApJ*, **530**, 1
Mirocha, J., Mason, C., & Stark, D. P. 2020, *MNRAS*, **498**, 2645
Morishita, T., Trenti, M., Stiavelli, M., et al. 2018, *ApJ*, **867**, 150
Naidu, R. P., Tacchella, S., Mason, C. A., et al. 2020, *ApJ*, **892**, 109
Oesch, P. A., Bouwens, R. J., Illingworth, G. D., et al. 2013, *ApJ*, **773**, 75
Oesch, P. A., Montes, M., Reddy, N., et al. 2018, *ApJS*, **237**, 12
Oesch, P. A., van Dokkum, P. G., Illingworth, G. D., et al. 2015, *ApJL*, **804**, L30
Oliphant, T. E. 2007, *CSE*, **9**, 10
Ota, K., Iye, M., Kashikawa, N., et al. 2008, *ApJ*, **677**, 12
Ota, K., Iye, M., Kashikawa, N., et al. 2010, *ApJ*, **722**, 803
Ota, K., Iye, M., Kashikawa, N., et al. 2017, *ApJ*, **844**, 85
Ouchi, M., Shimasaku, K., Akiyama, M., et al. 2008, *ApJS*, **176**, 301
Ouchi, M., Shimasaku, K., Furusawa, H., et al. 2010, *ApJ*, **723**, 869
Oyarzún, G. A., Blanc, G. A., González, V., et al. 2017, *ApJ*, **843**, 133
Partridge, R. B., & Peebles, P. J. E. 1967, *ApJ*, **147**, 868
Pérez, F., & Granger, B. E. 2007, *CSE*, **9**, 21
Planck Collaboration, Ade, P. A. R., Aghanim, N., et al. 2016, *A&A*, **594**, A13
Rauch, M., Haehnelt, M., Bunker, A., et al. 2008, *ApJ*, **681**, 856
Rhoads, J. E., & Malhotra, S. 2001, *ApJL*, **563**, L5
Robitaille, T. P., Tollerud, E. J., Greenfield, P., et al. 2013, *A&A*, **558**, A33
Ryan, R., Malhotra, S., Pirzkal, N., et al. 2019, *BAAS*, **51**, 413
Santos, S., Sobral, D., & Matthee, J. 2016, *MNRAS*, **463**, 1678
Schechter, P. 1976, *ApJ*, **203**, 297
Schenker, M. A., Ellis, R. S., Konidaris, N. P., & Stark, D. P. 2014, *ApJ*, **795**, 20
Schmidt, K. B., Treu, T., Trenti, M., et al. 2014, *ApJ*, **786**, 57
Shapley, A. E., Steidel, C. C., Pettini, M., & Adelberger, K. L. 2003, *ApJ*, **588**, 65
Shibuya, T., Kashikawa, N., Ota, K., et al. 2012, *ApJ*, **752**, 114
Shibuya, T., Ouchi, M., Konno, A., et al. 2018, *PASJ*, **70**, S14
Sobacchi, E., & Mesinger, A. 2015, *MNRAS*, **453**, 1843
Spergel, D., Gehrels, N., Breckinridge, J., et al. 2013, arXiv:1305.5425
Stark, D. P., Ellis, R. S., Chiu, K., Ouchi, M., & Bunker, A. 2010, *MNRAS*, **408**, 1628
Stark, D. P., Ellis, R. S., & Ouchi, M. 2011, *ApJL*, **728**, L2
Stern, D., Yost, S. A., Eckart, M. E., et al. 2005, *ApJ*, **619**, 12
Tacchella, S., Bose, S., Conroy, C., Eisenstein, D. J., & Johnson, B. D. 2018, *ApJ*, **868**, 92
Tacchella, S., Trenti, M., & Carollo, C. M. 2013, *ApJL*, **768**, L37
Taylor, A. J., Barger, A. J., Cowie, L. L., Hu, E. M., & Songaila, A. 2020, *ApJ*, **895**, 132
Tilvi, V., Pirzkal, N., Malhotra, S., et al. 2016, *ApJL*, **827**, L14
Tilvi, V., Rhoads, J. E., Hibon, P., et al. 2010, *ApJ*, **721**, 1853

- Trenti, M., & Stiavelli, M. 2008, [ApJ](#), **676**, 767
- Trenti, M., Stiavelli, M., Bouwens, R. J., et al. 2010, [ApJL](#), **714**, L202
- Treu, T., Schmidt, K. B., Trenti, M., Bradley, L. D., & Stiavelli, M. 2013, [ApJL](#), **775**, L29
- Urrutia, T., Wisotzki, L., Kerutt, J., et al. 2019, [A&A](#), **624**, A141
- Van Der Walt, S., Colbert, S. C., & Varoquaux, G. 2011, [CSE](#), **13**, 22
- Wang, F., Davies, F. B., Yang, J., et al. 2020, [ApJ](#), **896**, 23
- Weinberger, L. H., Haehnelt, M. G., & Kulkarni, G. 2019, [MNRAS](#), **485**, 1350
- Weinberger, L. H., Kulkarni, G., Haehnelt, M. G., Choudhury, T. R., & Puchwein, E. 2018, [MNRAS](#), **479**, 2564
- Whitler, L. R., Mason, C. A., Ren, K., et al. 2020, [MNRAS](#), **495**, 3602
- Wyithe, J. S. B., Yan, H., Windhorst, R. A., & Mao, S. 2011, [Natur](#), **469**, 181
- Zheng, Z.-Y., Wang, J., Rhoads, J., et al. 2017, [ApJL](#), **842**, L22